1   **Feldspar alteration by disequilibrium CO_2-H_2O fluids in reservoir sandstones:**
2   **Implications for CCS**

3   Authors: Natalie. J.C. Farrell[1], Lining Yang[2], Michael. J. Flowerdew[3], Chris Mark[4,5], Buhari
4   Ardo[1], Kevin. G. Taylor[1], Nico Bigaroni[1], Michael. Pointon[3], Lewis Hughes[1], John Waters[1],
5   Lee Paul[1]

6   1. Department of Earth and Environmental Sciences, Williamson Building, University of
7   Manchester, Manchester, United Kingdom
8   2. Institute of Marine Sciences (CNR-ISMAR), Bologna, Italy
9   3. CASP, Cambridge, United Kingdom
10   4. Department of Geology, Swedish Museum of Natural History, Stockholm, Sweden
11   5. School of Earth Sciences, University College Dublin, Ireland

12   *Corresponding author e-mail address: natalie.farrell@manchester.ac.uk. Co-author email
13   addresses: li-ning.yang@outlook.com, michael.flowerdew@casp.org.uk, chris.mark@nrm.se,
14   buhari.ardo@gmail.com, kevin.taylor@manchester.ac.uk, nico.bigaroni@manchester.ac.uk,
15   michael.pointon@casp.org.uk, lewis.hughes@manchester.ac.uk,
16   john.waters@manchester.ac.uk, lee.s.paul@manchester.ac.uk,

17   Keywords: Feldspar, CCS, Sandstone, reaction texture, dissolution, precipitation, calcite
18   cement

19   **Abstract [288/300]**

20   Understanding how the minerals in reservoir rocks respond to CO_2 injection is vital for the
21   success and safety of Carbon Capture and Storage (CCS) projects. Feldspars are the most
22   common mineral in the Earth's crust and act as primary framework grains in sandstones.
23   Compared to quartz, feldspars are mechanically weak and chemically reactive. Dissolved
24   feldspars can re-precipitate as clays, which in CCS reservoirs could impact fluid-flow. While
25   caprock mineral stability is well studied, reservoir mineral reactivity, particularly of feldspars,
26   remains understudied. To address this knowledge gap, we present microstructural and
27   geochemical data from batch experiments that reacted CO_2-enriched fluids with feldspar-
28   bearing sandstone sampled from the Captain Sandstone Member, the primary reservoir for the
29   Acorn CCS Project (UK).

30   Experiments were conducted in a hydrostatic pressure vessel at 70 MPa confining pressure, 50
31   MPa pore pressure, and temperatures ranging from 80°C to 550°C, using CO_2-enriched water

to simulate reservoir conditions. Pre- and post-reaction samples were analysed using XRD, SEM-EDS, and XCT to assess microstructural and mineralogical changes. Results show that CO_2:feldspar interactions differ significantly from control experiments involving water alone. At reservoir-relevant temperatures (80°C), incongruent dissolution of K-feldspar weakened grains which led to microfracturing. At 250°C, CO_2 fluids caused total dissolution of calcite grains and cement and selective leaching of calcium from oligoclase, enriching the pore fluid with Ca^{2+}. Above 400°C, coupled dissolution–precipitation processes were observed, including congruent K-feldspar dissolution, secondary porosity development, and localised precipitation of Ca-aluminosilicates and K-bearing phases around dissolving K-feldspars. These transformations could alter reservoir flow pathways and induce mechanical risks, i.e. destabilising nearby faults or initiating reservoir collapse. Given feldspars' prevalence in crustal rocks and CCS sandstone reservoirs, their reactive behaviour under in-situ conditions and in the presence of aggressive fluids demands greater attention.

1. Introduction

Carbon Capture and Storage (CCS) projects aim to moderate the impacts of climate changes by injecting supercritical CO_2 into porous rock, such as deep saline aquifers and depleted hydrocarbon sandstone reservoirs, where it is intended to be stored for 10,000 years/indefinitely (IPCC, 2005). The productivity and safety of CCS projects hinge on our ability to efficiently flow CO_2 fluids into subsurface rock formations while preventing leakage. A key challenge for success is the ability to predict dynamically changing fluid-flow during injection and CO_2 plume migration (Juanes et al, 2006; Benson and Cole, 2008; Ringrose, 2020). This requires both a specific knowledge of the pre-injection micro-scale reservoir properties, e.g., pore volume, pore connectivity, grain texture, and a broader empirical understanding of how injected fluids might mechanically and/or chemically alter this microstructure and thereby impact CCS project efficiency and safety (Rochelle et al, 2004; Hall et al, 2015; Rathnaweera et al, 2015; Shogenov et al, 2015; Fuchs et al, 2019; Foroutan et al, 2021; Pessu et al, 2025). Experimental studies have explored these CO_2-fluid-sandstone interactions showing that the acidic brines created by dissolution of CO_2 into formation fluids enhances dissolution of carbonate minerals, primarily as cements in sandstone reservoirs (Ross et al, 1982; Bertier et al, 2006; Hangx et al, 2013) with fewer studies reporting CO_2 fluid alteration of reactive aluminosilicates, including feldspars (Bertier et al, 2006; Hall et al, 2015; Lu et al. 2013). Geochemical models indicate that feldspar alteration may result in precipitation

64 of carbonate minerals e.g., dolomite and dawsonite, which could permanently 'lock-in' CO_2

65 (Durst et al., 2000, Seisenbayev et al, 2023). Feldspar:CO_2 reactivity could substantially

66 influence the performance and stability of CCS reservoirs, yet their response to saturation with

67 CO_2-enriched fluids under reservoir conditions (temperature *and* stress), including reaction

68 types and rates and the consequences of reactivity, is poorly understood (Lu et al. 2013). This

69 is a key knowledge gap especially in polymineralic rocks like sandstone where coupled

70 chemical–mechanical processes are already poorly constrained.

1.1. *Feldspar solubility*

72 Feldspars are a volumetrically significant, mechanically weak and chemically reactive

73 framework mineral in sandstones (Tullis and Yund, 1977) and most crustal rocks. In

74 comparison to quartz, feldspars are highly reactive (Knauss and Wolery, 1986; Dove and

75 Crerar, 1990). They can dissolve creating significant secondary porosity (Farrell and Healy,

76 2017) and re-precipitate as clays, which impede fluid-flow and mechanically weaken rocks

77 (Farrell et al, 2021; Summers and Byerlee, 1977; Collettini et al, 2019 respectively), outcomes

78 that could compromise both CCS reservoir efficiency and mechanical integrity. Feldspar

79 solubility is strongly influenced by pH, as demonstrated in early experimental studies (Correns,

80 1961; Wollast, 1967). These investigations established that feldspar dissolution rates increase

81 significantly under acidic conditions due to enhanced hydrolysis of Si–O and Al–O bonds in

82 the crystal lattice, the rate of which is determined by grain surface area (Helgeson et al, 1984).

83 Feldspars are mineralogically well defined, but their subsurface behaviour is uncertain. As key

84 framework minerals in many of Earth's oldest crustal rocks e.g., gneisses, granites and

85 sandstones, they can preserve evidence of their extensive geological histories (e.g. weathering,

86 transport, burial, fluid interaction), which are reflected in their diverse microstructural textures

87 and chemical heterogeneity. This inherited heterogeneity directly affects their reactivity.

88 Across kilometre-scale reservoirs, their solubility can differ significantly based on provenance

89 (detrital sources) and their burial or fluid-flow history (Glasmann, 1992), making some grains

90 more or less prone to dissolution. Chemical alteration has been shown to enhance stress-

91 corrosion cracking in quartz (Scholz, 1972), hence deformation of more reactive feldspars (via

92 chemical dissolution and mechanical cracking) in the presence of chemically active CO_2 fluids

93 is expected.

1.2. *Predicting feldspar reaction rates*

95   Mineral reaction rates are typically defined by experiments on powdered rock samples
96   (Brantley et al, 2008). While using powders allows for control over reactant surface area, this
97   method fails to account for the grain-to-grain stresses present in subsurface rocks. Even in
98   hydrostatic experiments, such stresses at the grain scale can significantly accelerate mineral
99   dissolution rates, often exceeding predictions based on powder-derived rate laws (Rutter, 1976;
100   Wheeler, 1991). Considering the inherent weakness of feldspars under pressure-temperature
101   conditions in the shallow crust, these stresses could induce microfracturing, which increases
102   surface area and exposes fresh reactive surfaces that drive further reaction. Geochemical
103   simulations frequently oversimplify feldspars, disregarding their diverse chemical
104   compositions and variable textures i.e., surface areas, which are crucial for accurate reaction
105   rate predictions (Helgeson et al, 1984). Enhanced understanding of feldspars, from quantifying
106   the compositional variability in target reservoirs, to empirical evidence of feldspar:CO_2
107   reactions i.e., dissolution rates and secondary mineral formation, should improve the accuracy
108   of geochemical and reactive transport models. We hypothesise that injection of CO_2 enriched
109   fluids will impact the solubility of *stressed* feldspar grains and potentially alter the properties
110   of sandstone CCS reservoirs, specifically the pore volume, pore connectivity, permeability and
111   geomechanical stability.

112   This paper presents microstructural insights from a suite of coupled chemical:mechanical
113   reaction experiments on feldspar-bearing sandstones from the Early Cretaceous Captain
114   Sandstone Member from the Moray Firth, Scotland, the target reservoir for the Acorn CCS
115   Project (Alcalde et al, 2019), highlighting the impact of CO_2 fluid saturation on reactive
116   framework grains under subsurface conditions. In this study we used an externally heated,
117   hydrostatic pressure vessel to investigate the solubility of various feldspars in a CO_2 saturated
118   sandstone under hydrostatic stress, simulating CCS reservoir conditions in closed batch system
119   experiments. Experiments were conducted at a range of increasing temperatures, effectively
120   accelerating reaction rates simulating mineral reactions over hundreds of years – aligning with
121   the timescales required for CO_2 storage. The temperature dependence of mineral dissolution
122   follows an Arrhenius relationship, linking the reaction rate constant to temperature. For K-
123   feldspar, the baseline rate constant is well-established, and we approximate its temperature
124   dependency using established rate laws for dissolution in varying pH fluids (Helgeson, 1984;
125   Blum and Stillings, 1995). Unlike previous Captain Sandstone experimental studies that
126   focused solely on reservoir mechanical stability using water as a pore fluid at ambient
127   temperatures (Allen et al, 2020) or on the mechanical impact of CO_2 fluids on carbonate cement

128 dissolution at low temperatures in an open pore fluid system (Hangx, 2013), this research
129 explores the role of CO_2 fluid chemistry on the dissolution and stress-induced deformation of
130 arguably more important *framework* grains over geological timescales. These results address a
131 major knowledge gap in CCS reservoir appraisal and have scope to provide empirical
132 constraints for long-term CO_2 containment predictions.

133 **2. Material and Methods**

134 This study used an overlapping programme of experimental rock deformation, microstructural
135 and geochemical analysis to characterise the range/integrity of feldspars contained in a CCS
136 target sandstone samples in the context of the reservoir geological history; experimentally
137 assess how feldspars interact with CO_2-enriched fluids under subsurface conditions
138 (temperature, pressure and grain scale stress) and consider the effect of feldspar dissolution
139 and subsequent precipitation of clay minerals on reservoir properties of fluid-flow and
140 mechanical strength. The characterisation of pre-experiment, in situ Captain Sandstone
141 feldspars is summarised in Section 2.1 and reported along with a compositional analysis and a
142 provenance model for direct and recycled feldspars by Flowerdew et al., 2024.

143 *2.1. Material*

144 Core plugs used in these experiments were taken from two sites within the historic petroleum
145 well (14/29a-5, Goldeneye Field, around 8500 ft/2590.8 m), specifically from the D sand top
146 and D sand middle intervals. These sandstones form the target 'D sand' unit of the planned
147 CO_2 storage reservoir at the Acorn CO_2 storage site, Scotland (Alcalde et al., 2019). The
148 principal reservoir consists of fine to medium grained, high porosity, subarkosic turbidite
149 deposits (Pinnock et al, 2003; Stewart and Marshall, 2020). Detrital mineralogy is dominated
150 by quartz, plagioclase (albite and oligoclase) and orthoclase with some mica, glauconite and
151 mudclasts. Some feldspars in the 'D sand' subdivision of the Member have already been very
152 reactive as shown by secondary porosity (Stewart and Marshall, 2020), more prominent at its
153 top.

154 Captain Sandstone 'D sand' samples comprise poorly cemented subarkose (Folk et al, 1970).
155 Thin section analysis showed that grains are moderately to poorly sorted, 50 to >1000 μm in
156 diameter and loosely packed with around 30% pore area. Intergranular pores are large and
157 irregular or smaller and angular formed by the intersections of multiple rounded grains (Fig
158 1.a). X-ray diffraction analysis showed that samples broadly contain 76% quartz, 8%

plagioclase, 8% K-feldspar, 6% clays, predominantly kaolinite plus minor amounts of 1% calcite, 1% glauconite (XRD method and results, Table 2, Supp. Mat,). Mineralogical makeup was also determined by using element data obtained from scanning electron microscopy energy dispersive X-ray spectroscopy (hereafter abbreviated to EDS) mapping overlain on Backscattered electron images (BSE) taken using a Scanning Electron Microscope (SEM) (Fig 1.b).
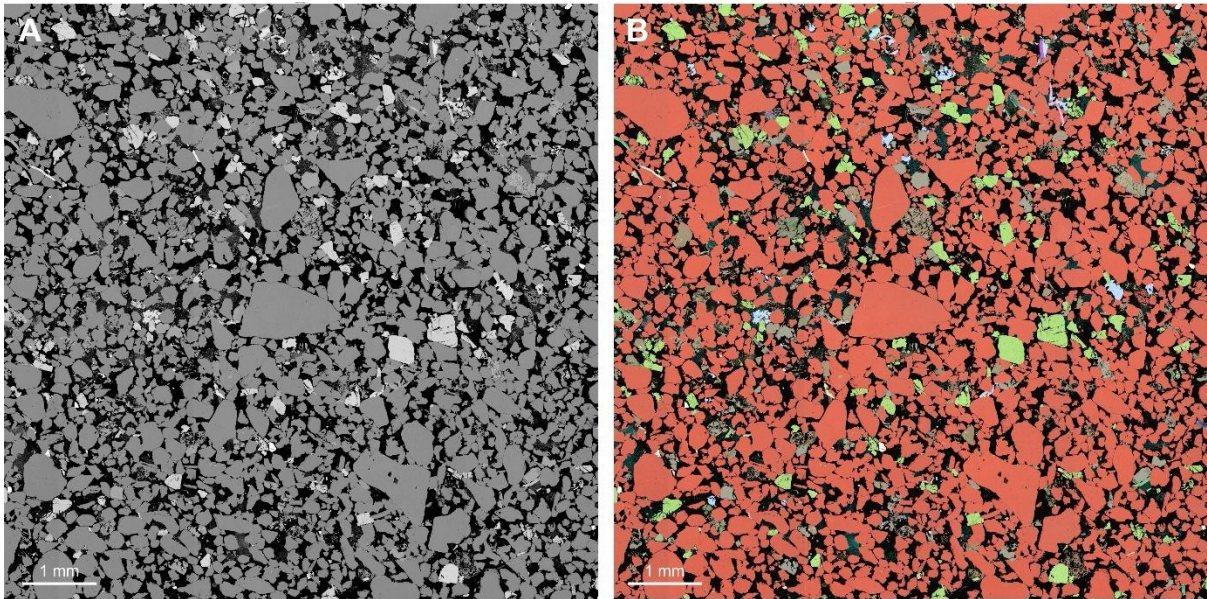
Fig 1. Back scattered Electron and semi-transparent EDS elemental maps of pre-experiment D sand, Captain Sandstone (a and b respectively). Black = pore/void space, red/orange = quartz, green/yellow = orthoclase, grey/brown = oligoclase, pale blue = calcite

Captain Sandstone feldspars are mineralogically and texturally diverse showing three dominant mineralogies; two plagioclases, intermediate NaCa bearing oligoclase and end member Na-rich albite and K-feldspar (Figure 2.a - e). The reactivity of plagioclase is already apparent in the pre-experiment samples, as indicated by the skeletal texture of albite grains (Fig. 2.b). This texture likely results from the albitisation of oligoclase, driven by chemical exchange where Ca in oligoclase is replaced by Na from brines, substituting Ca^{2+} ions with Na^+, and releasing Ca^{2+} into the fluid (Fig. 2.c). Additionally, plagioclase reaction and dissolution (whether oligoclase or albite) has likely released Al and Si to form kaolinite precipitates during geological diagenesis (Figs. 2.b and c). Both plagioclase and oligoclase grains commonly range between ~100 – 200 μm diameters and display blocky, sub-rectangular grain boundaries with rounded edges (Fig. 3, Supp. Mat,). K-feldspars tend to be larger than plagioclases, averaging 200-300 μm diameter and display coherent, rounded grain boundaries abutting similarly shaped quartz grains (Fig 2.c). Many K-feldspars show perthite textures with darker fine bands and streaks of albite lamellae oriented along cleavage planes (Fig 2.d and Fig 3. Supp. Mat,). Some

183 K-feldspars show reaction in perthite grains with some preferential dissolution of albite
184 lamellae and opening up of intergranular porosity along these features (Fig. 2.f).
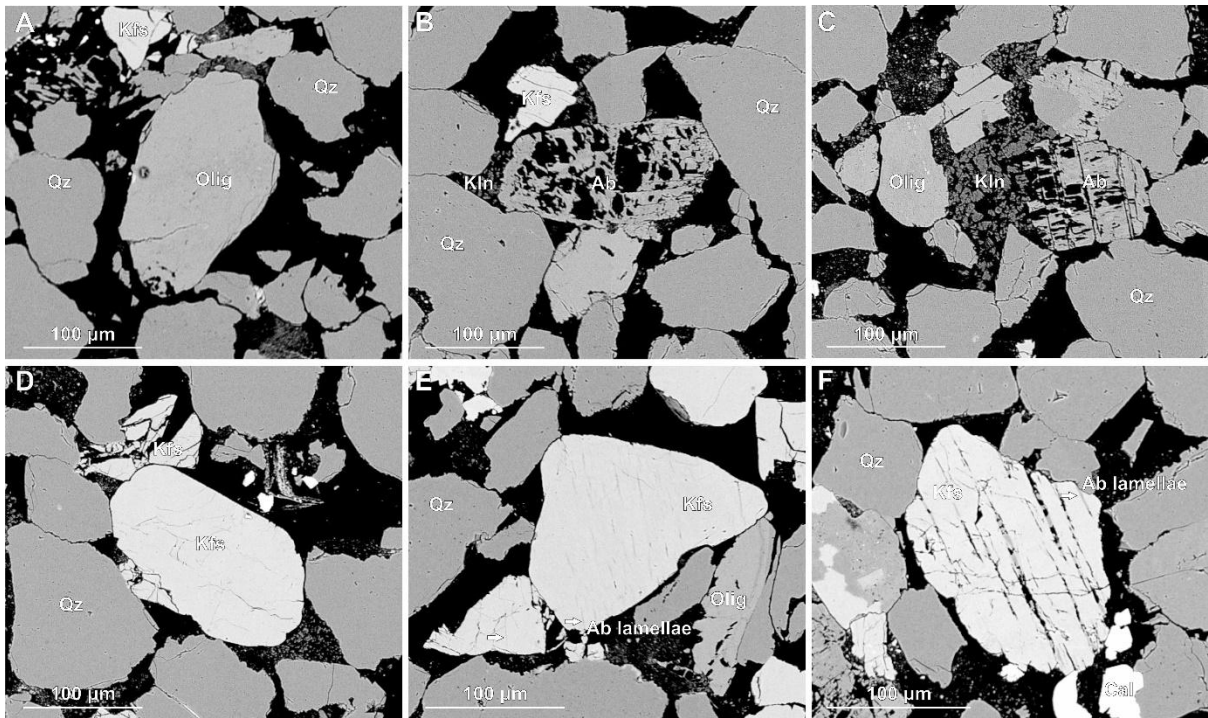
185

186 **Figure 2. Back Scattered Electron images showing feldspar types including plagioclases, oligoclase (a and**
187 **c) and albite (b and c) and K- feldspar (d-f) in pre-experiment samples of Captain Sandstone. Abbreviations**
188 **follow Whitney and Evans, 2010. Quartz (Qz), (Oligoclase (Olig), K-feldspar (Kfs), Albite (Ab), Kaolinite**
189 **(Kln).**

190 *2.2. Experimental method*

191 Eight reaction experiments were performed on 9.5 mm diameter core plugs of Captain
192 Sandstone Member 'D sand' using hydrostatic pressure vessels at ~70 MPa confining pressure
193 (Pc) aka ~3 km burial depth with 50 MPa pore fluid pressure (Pf). Four experiments used CO_2
194 saturated water as a pore fluid (as a proxy for CO_2 injection), while four control experiments
195 used H_2O under the same conditions. We experimentally modelled the progression of feldspar
196 reactivity under subsurface conditions by conducting experiments across a range of
197 temperatures (from 80°C, aka reservoir conditions, up to 550°C), using elevated temperatures
198 as a proxy for longer reaction time. This approach uses the Arrhenius equation, which describes
199 the temperature dependence of reaction rates, allowing higher temperatures to accelerate
200 mineral reactions and simulate longer-term geochemical processes within practical and
201 repeatable laboratory timescales (calculated reaction rate ratios for these experiments detailed
202 in Supp. Mat.). These results can then be extrapolated to reservoir temperatures following
203 standard practice in mineral-reaction studies (Blum and Stillings, 1995), a methodology
204 commonly used to model reservoir evolution over geological timescales (Brantley et al, 2008;

7

205 Hangx and Spiers, 2009; Hellmann et al., 2012). Experimental conditions are detailed in Table

206 1.

Sample ID	Rig ID	Pore Fluid Chemistry	Temperature (°C)	Confining Pressure (MPa)	Pore Fluid Pressure (MPa)	Duration (days)
Dt02	Nimonic 3	H_2CO_3	80	70	50	6
Dm07	Nimonic 2	H_2O	80	70	50	6
Dt01	Nimonic 3	H_2CO_3	250	70	50	10
Dm04	Nimonic 2	H_2O	250	77	50	10
Dt03	Nimonic 3	H_2CO_3	400	70	50	6
Dm06	Nimonic 2	H_2O	400	75	50	6
Dm01	Nimonic 3	H_2O	550	72	50	6
Dm05	Nimonic 3	H_2CO_3	550	80	50	6

207
208 **Table 1. Experimental conditions for batch reactor tests conducted in triaxial deformation rigs 'Nimonic**
209 **2' and 'Nimonic 3'. Core plugs of Captain Sandstone were reacted with differing pore fluid chemistries**
210 **under constant Pf, Pc and temperatures for durations of 6-10 days with the objective of assessing the**
211 **influence of pore fluid chemistry and temperature on mineral stability and microstructure.**

212 Experiments were conducted using externally heated triaxial deformation apparatus, 'Nimonic

213 2' and 'Nimonic 3'. The pressure vessel and sample assembly in these rigs are constructed

214 from nickel alloy (Nimonic® 115) which is highly resistance to oxidation and compatible with

215 carbonic acid and other corrosive fluids at elevated temperatures, preventing piston reactions

216 that could contaminate the rock sample (Fig 3). Samples were contained within annealed

217 copper jackets to isolate them from the water confining fluid, which was pressurised to

218 reservoir conditions using a compressed air pump. Both Pc and Pf were gradually increased in

219 succession up to the required experiment conditions to prevent pore collapse and preserve the

220 starting material grains and microstructure. For control experiments, the pore fluid was tap

221 water (very soft with total hardness of 16 mg/L, Supp. Mat, Table 1), while for CO_2 proxy

222 experiments, the same water was saturated with CO_2 using a SodaStream®. The resulting 'fizzy

223 water' contained ~6 g/L CO_2, yielding a pH of 4. Pf was controlled using a pore volumometer

224 with a piston driven by a DC servo-motor. This system allowed precise adjustments of the

225 piston in and out of a 3 cm³ pressure vessel to maintain a constant Pf through feedback control

226 from a pore pressure transducer. A 50 MPa Pf was used in all experiments to ensure that water

227 remained in a liquid state even above its critical point ~400°C, thereby preserving consistent

228 stress conditions throughout the experiments. Once at pressure, the experiment temperature

229 was applied using upper and lower external furnaces which create a thermal gradient which

230 can be used to position a 'hot spot' within the pressure vessel focused around the relatively

231 small sample. The furnace temperature was increased to the required level using variacs, which

232 control the voltage to the furnaces for precise adjustments. The temperature was then

233 maintained at the set value for six days with stable power regulation from the variacs. Sample
234 temperature was monitored using an inconel-sheathed thermocouple inserted down the upper
235 piston. Pre experiment calibrations showed a temperature range of <2°C along the sample
236 length at 500°C. Experiments were ended by decreasing temperature back to ambient
237 conditions then unloading the Pf and Pc in tandem and in reverse to protect the pore space.
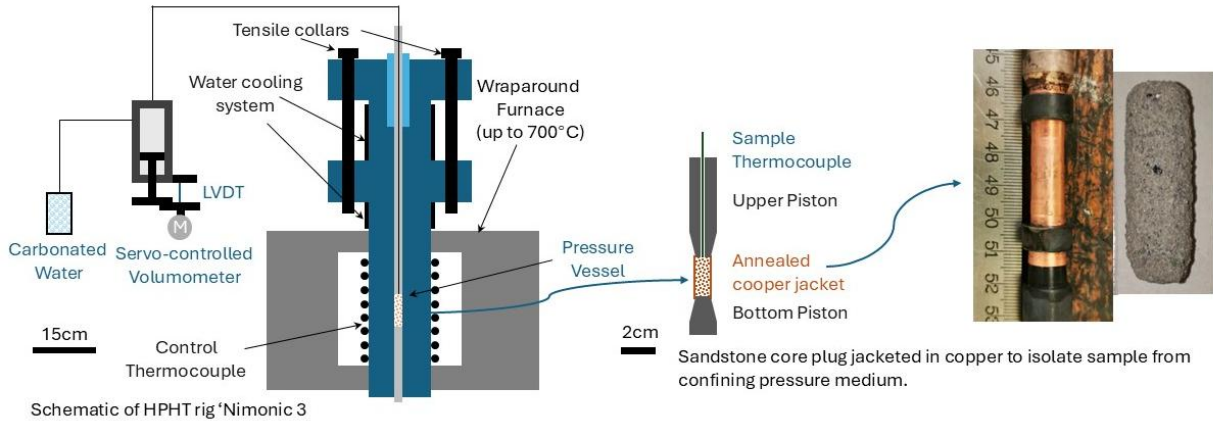
238
239 **Figure 3. Schematic cross section diagram of high pressure, high temperature triaxial rig 'Nimonic 3'**
240 **illustrating the sample assembly within the Nimonic pistons (rhs), confinement of sample with the pressure**
241 **vessel and furnace (centre) and pore volumometer controlling injection and pressure of pore fluid along**
242 **the top piston (lhs).**
243

244 *2.3. Microstructural analysis*

245 Post experiment jacketed core plugs were injected with epoxy under a vacuum and then halved
246 to make thin sections covering the central portion of the sample cylinder. Polished sections
247 were carbon coated before being imaged using a Zeiss Evo MA 15 scanning electron
248 microscope housed at CASP. Back scattered electron (BSE) images and elemental maps were
249 collected using one or a combination of a Zeiss Back Scatter Electron (BSE) detector, an
250 Oxford Instruments Ultim Max 100 Energy dispersive x-ray spectrometer (EDS) detector and
251 an Oxford Instruments Unity detector. Montages of images that cover the thin section were
252 collected at 20 kV and 2000 pA probe current, and 10 kV and 200 pA probe current where
253 greater definition imagery was required. Images and data were collected, manipulated and
254 exported using Oxford Instruments AZtec software version 6.1, coupled with the
255 AutoPhaseMap and AZtecFeature analysis and CASP's in-house mineral classification
256 scheme.

257 Microstructural analysis was conducted on BSE and EDS images of pre- and post-experiment
258 thin sections to examine and characterise mineral phases and textures and analyse reaction
259 pathways between grains. This analysis was facilitated by the generation of EDS x-ray spectra

for specific points or regions on the map. Post experimental mineral dissolution and/or precipitation was quantified from BSE maps overlain with semi-transparent EDS maps by thresholding the area covered by key mineral phases (K-feldspar, plagioclase, calcite) using image analysis software ImageJ and defining this result as a percentage of the total grain content (see Section 1.4, Supp. Mat, for more information). Individual montage images were analysed separately to investigate the heterogeneity of pore and grain distributions (as per method in Farrell and Healy, 2017). Additional 3D micro-CT images were produced of pre and post experiment samples to assess grain deformation and pore networks. The micro-CT data had limited resolution compared to the SEM data and so are not discussed here but are included in the Supplementary Materials.

3. Results

Microstructural and compositional changes were identified in all experimentally reacted samples indicating cation exchange between pore fluid and sandstone samples after experimental run times of six days. The experimental duration, stress conditions and pore fluid compositions are summarised in Table 1. In this section we present petrographic results for specific mineral phases and their alteration in the presence of CO_2-enriched water compared with H_2O (i.e. tap water) (Fig 4-10). Image analysis was used to quantify the extent of mineral alteration in post-experiment samples compared to pre-experiment. Mineral quantifications are presented as box plots to show changes in mean mineral content which could be used in geochemical models and to illustrate the statistical distribution and variability of mineral grains within samples, highlighting dissolution heterogeneity (Fig 11). Additional microstructural data from all experiments are shared in a Supplementary Materials document (Supp. Mat.).

3.1. Alteration of K-feldspar

3.1.1. K-feldspar:CO₂ enriched pore fluids

Post-experiment BSE imaging reveals significant microstructural changes in K-feldspar grains reacted at different temperatures. Compared to pre-experiment samples, which exhibit minimal fracturing (Fig. 2.d-f, and Supp. Mat. Fig. 3), post-experiment K-feldspar grains display dissolution, systematic microfracturing and grain fragmentation and development of secondary porosity providing evidence of active mineral alteration during experiments (Fig. 4; Supp. Mat. Figs. 5–8).

290   At 80°C, open pores develop on grain surfaces as linear and parallel 'cracks' or 'seams' that
291   propagate into grain interiors at high angles, often forming bimodal cross-cutting sets aligned
292   with cleavage planes (Fig. 4.a–b; Supp. Mat. Figs. 5–6) and commonly oriented with albitised
293   lamellae (Fig. 5.a). Some tightly packed K-feldspars are fractured against adjacent grains and
294   crushed between quartz grains, which remain largely intact, suggesting mechanical weakening
295   of stressed K-feldspars, likely enhanced by localised dissolution and development of porous
296   'seams' on the grain edges (Supp. Mat. Fig. 5). At 250°C intergranular dissolution becomes
297   more pronounced, suggesting that increased intergranular fracture density both enhanced
298   reactive surface area and created conduits for further fluid-rock interaction (Fig. 4.c). At 400°C,
299   K-feldspar dissolution is accompanied by the formation of thin (~3 μm), discontinuous calcic
300   aluminosilicate overgrowths along open grain boundaries, particularly around smaller K-
301   feldspar fragments (Fig. 4.d; Fig. 5.b). EDS spot analysis shows overgrowths are chemically
302   equivalent to calcic plagioclase (andesine- anorthite) (Supp Mat. Fig 17). At 550°C,
303   intergranular fractures widen (5–10 μm vs. <5 μm at 400°C), and K-feldspars are segmented
304   by cross-cutting fractures into fragments with rounded, dissolution-modified edges (Fig. 4.e–
305   f). In this sample secondary porosity is widespread and these pores can often be identified by
306   "ghosts" of former grain outlines defined by secondary clay precipitates (Supp. Mat. Figs. 6–8
307   and XCT images and animations, https://doi.org/10.6084/m9.figshare.30061294.v1).
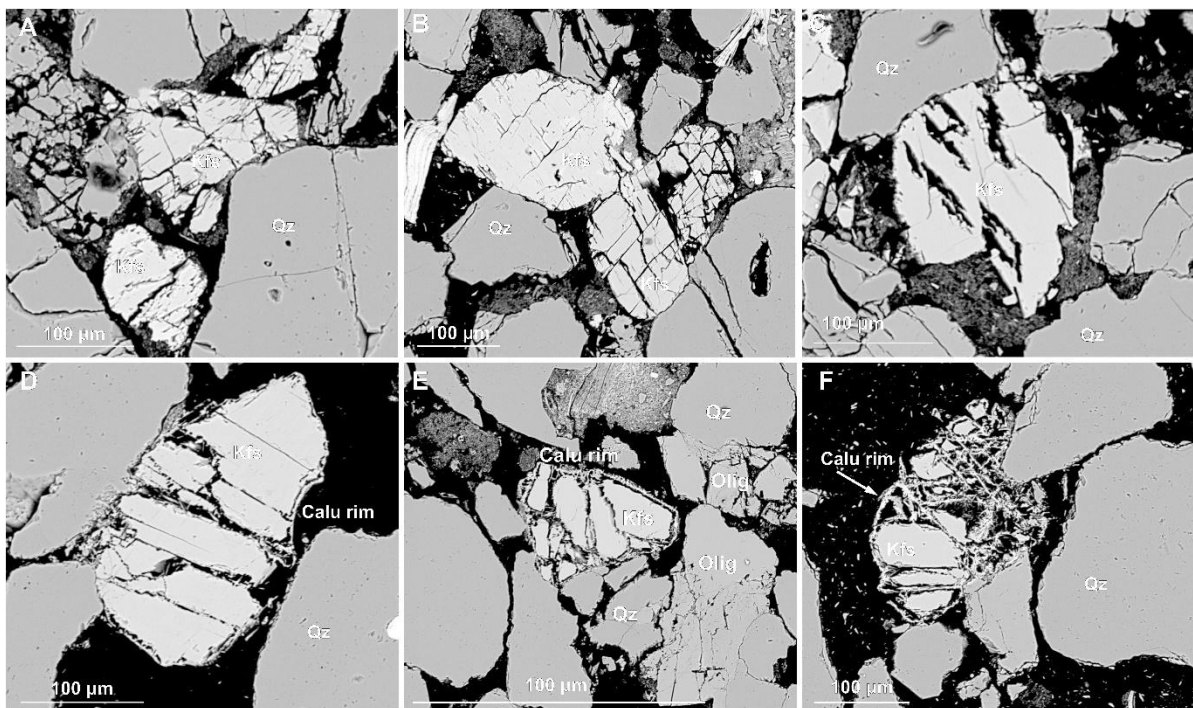
308
309   **Figure 4. Back scattered electron (BSE) images showing progressive K-feldspar (Kfs) alteration via**
310   **chemical and mechanical deformation with increasing temperature reaction experiments conducted with**
311   **CO_2 fluids at hydrostatic conditions, including – dissolution and grain microfracturing at experiments**
312   **conducted at 80°C (a and b), grain dissolution at 250°C (c), and secondary mineral growth around K-**

11

feldspar grains at 550°C (d - f). Quartz (Qz), (Oligoclase (Olig), K-feldspar (Kfs), Calcic aluminosilicate (Calu).

Secondary precipitation phases are most prominent at higher temperatures (400–550 °C), appearing as a Ca-rich pale blue and K-rich bright green phases in combined EDS-BSE images (Fig. 5). Precipitates are often located around 'free' edges of grains i.e. not in contact with adjacent grains and become thicker (~10 μm) and more continuous at 550°C, while grain to grain boundaries display concave-convex contacts with adjacent quartz grains, implying differential dissolution and possible influence of intragranular stress on reactivity (Fig. 5.c). Dissolved K-feldspar grain edges typically exhibit irregular, serrated morphologies (Fig. 5.d; Supp. Mat. Figs. 7–8). In some images, a narrow void separates receding K-feldspar grain edges from calcitic overgrowths, marking a zone where dissolution likely outpaced precipitation (Fig. 4.d–f; Fig. 5.c–d). High-magnification imaging shows outward nucleation of these calcic aluminosilicates at high angles from K-feldspar surfaces and aligned crystallographically with the host grain (Fig. 5.d). Thin K-feldspar strands remain linked to the overgrowths, suggesting ongoing elemental exchange. A K-rich phase, likely mica, is also observed as a bright green band within and beyond the pale blue rims, forming spindly, fibrous morphologies (Fig. 5.d). In the high temperature experiments, the K-rich phase is also precipitated in pore space and pore throats, within the clay masses small crystals of the calcic aluminosilicate has nucleated (Fig. 5.b).
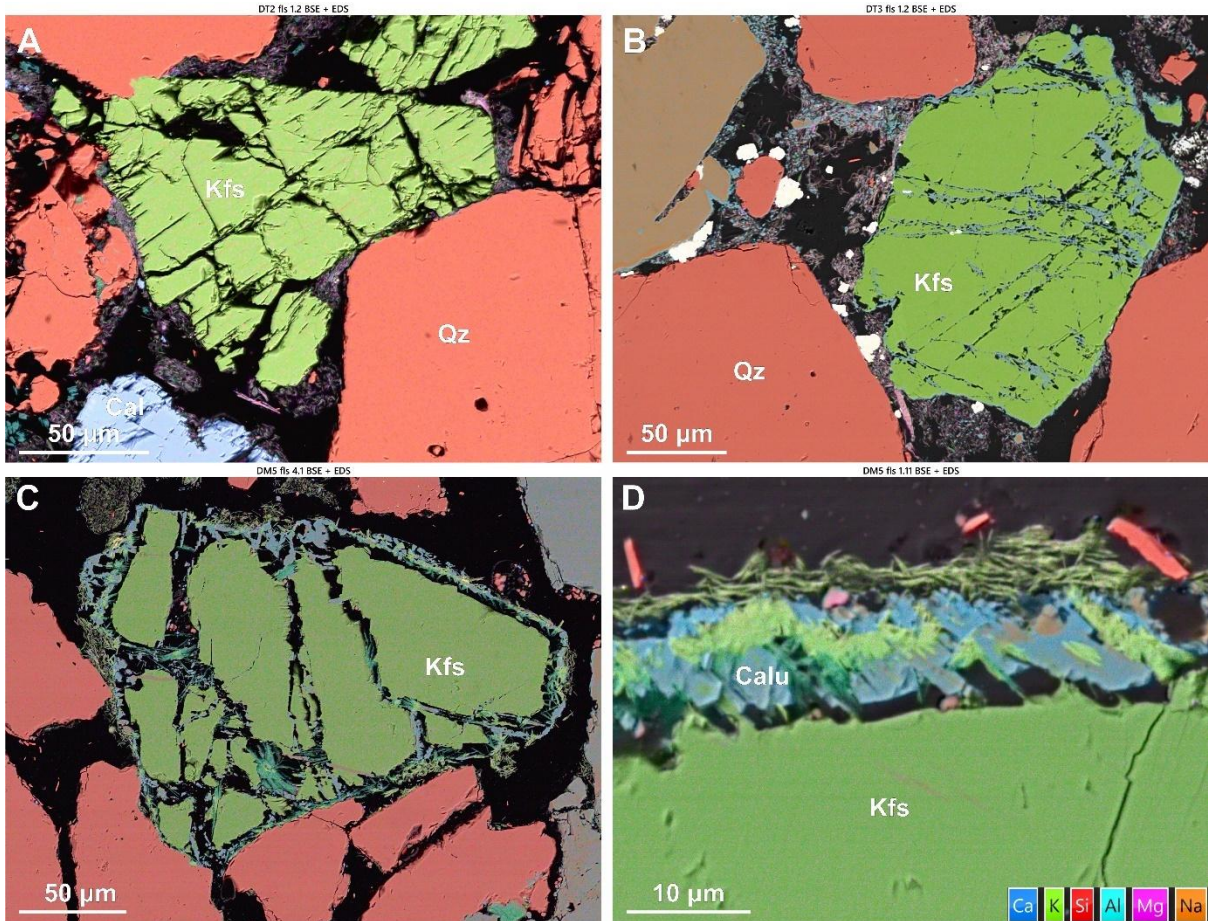
Figure 5. High-magnification backscattered electron (BSE) images, overlaid with semi-transparent elemental EDS maps, showing progressively enhanced microfracturing, dissolution, and secondary precipitation in K-feldspar saturated with CO2 enriched fluids at a range of experimental temperatures (80°C (a), 400°C (b), and 550°C (c, d).

3.1.2. K-feldspar:H_2O pore fluids

In H2O experiments (tap water as pore fluid), post-reaction samples show temperature-dependent microstructural changes distinct from those observed under CO_2-enriched fluid conditions. At 80°C, microfractures in K-feldspar are primarily grain-bound, with curvilinear to sub-parallel orientations (Fig. 6.c–d), the latter suggesting crystallographic control and possible mechanical weakening. These features differ from the chemically driven dissolution seams, serrated grain edges, and widening of intragranular fractures observed in the CO_2 experiments (Section 3.1.1). At higher temperatures 400°C, K-feldspars appear to have been mechanically weakened with post experiment samples showing enhanced intergranular fracturing, local grain crushing, and some convex–concave grain contacts. At 550°C, K-feldspars in H2O experiments exhibited irregular intergranular fracturing and precipitation of calcic aluminosilicate overgrowths and a K-rich phase which also formed discontinuous rims around grain edges (Fig. 6; Supp. Mat. Figs. 9–12). However, unlike the CO_2 experiments, these rims are thinner and more spatially limited, and K-feldspar dissolution features were less

13

pronounced. These contrasts highlight the influence of pore fluid chemistry on K-feldspar enhanced reactivity under CO_2-enriched conditions.
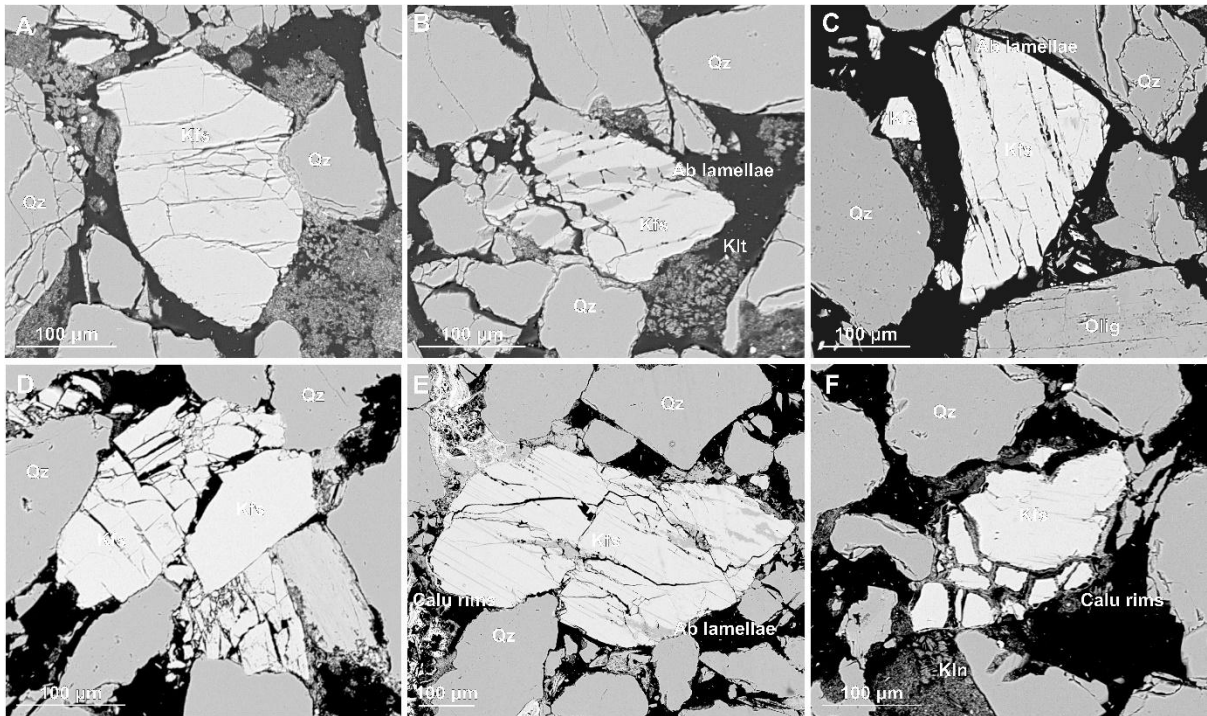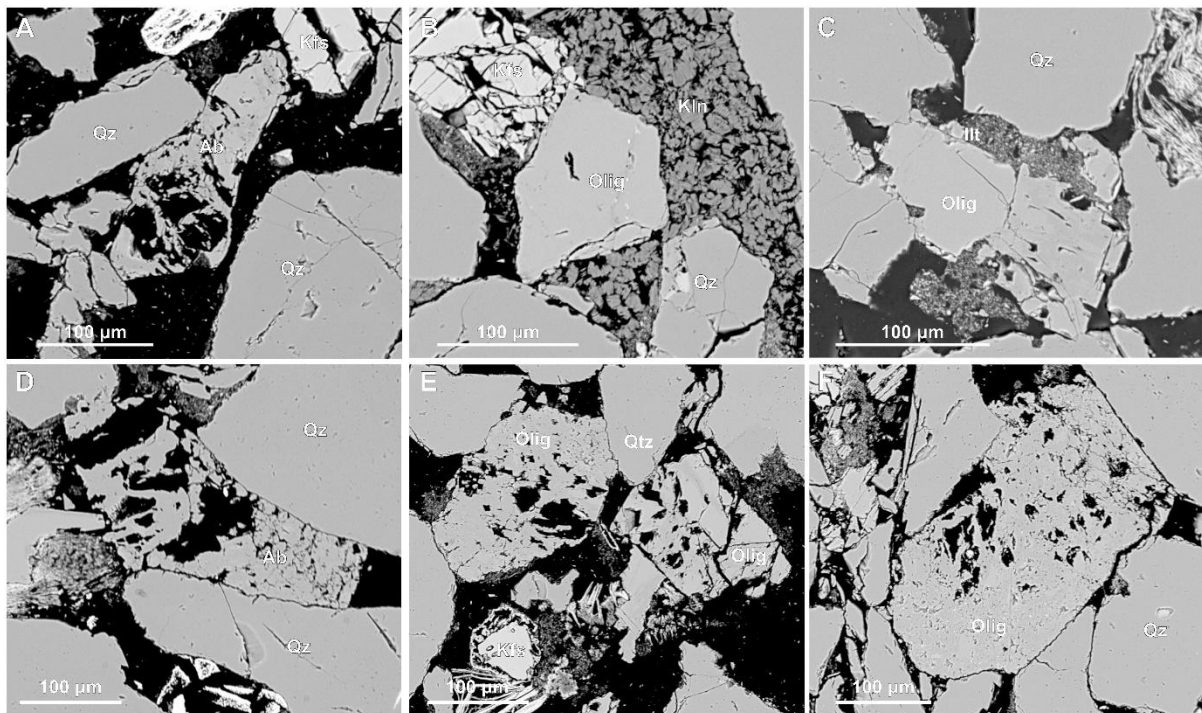

Figure 6. Back scattered electron images showing mechanical fracturing of K-feldspar grains in reaction experiments with H_2O pore fluid at 80°C (a and b), 250°C and 400°C (c and d) and 550°C (e and f). Fractures are generally grain bound with irregular, curvilinear traces and some crystallographic alignment at experiments conducted at higher temperatures (c and e) indicating mechanical weakening. Minimal K-feldspar dissolution and persistent presence of albite lamellae suggest reduced alteration under H_2O compared to CO_2-saturated conditions.

3.2. Alteration of plagioclase

3.2.1. Plagioclase:CO_2 enriched pore fluids

The Captain Sandstone Member contains two types of plagioclase: Na-rich end member albite and intermediate oligoclase (Fig 2). The impact of CO_2 enriched pore fluids on oligoclase and albite, is markedly different to each other. At 80°C (reservoir temperature) albite grains remain coherent/intact with their original grain boundaries and skeletal textures (Fig 7.a) while oligoclase grains show minor marginal dissolution or 'scalloping' along grain edges (Fig 7.b). At 250°C, oligoclase grains have complex, indented grain boundaries often surrounded by kaolinite and mixed-element fine clays (Fig. 7.b, c). Some grains show evidence of intergranular pore development or surface etching, though intergranular microfracturing is limited or absent. At higher temperatures (>400°C), intergranular porosity in oligoclase increases due to grain dissolution (Fig. 7.e, f). Albite grains also show significant intergranular

372   porosity, though this appears consistent with the skeletal textures observed in pre-experiment

373   sandstones (Fig. 7.d).

374
375   **Figure 7. Back scattered electron (BSE) images showing plagioclase grains post reaction experiment**
376   **condition with CO_2 enriched fluids. Images show no alteration of albite grains at 80°C or 550°C (a and d)**
377   **while oligoclase grains appear partially dissolved on the grain boundaries at 250°C and 400°C (c) and**
378   **etching and intergranular porosity at 550°C (e and f).**

379   Combined BSE and EDS images or oligoclase grains reacted at 400°C show leaching of Ca+

380   from grain edges leaving an original Na-Ca rich grain centre, a ~20-30 μm thick Na rich albitic

381   grain edge plus 2-5 μm calcium aluminosilicate rims similar to features observed on K-feldspar

382   grains but without the void space between the dissolving host grain and secondary precipitate

383   (Fig 8). In contrast, albite shows minimal evidence of chemical interaction with CO_2-enriched

384   fluids at any temperature (Fig. 7.a, d).
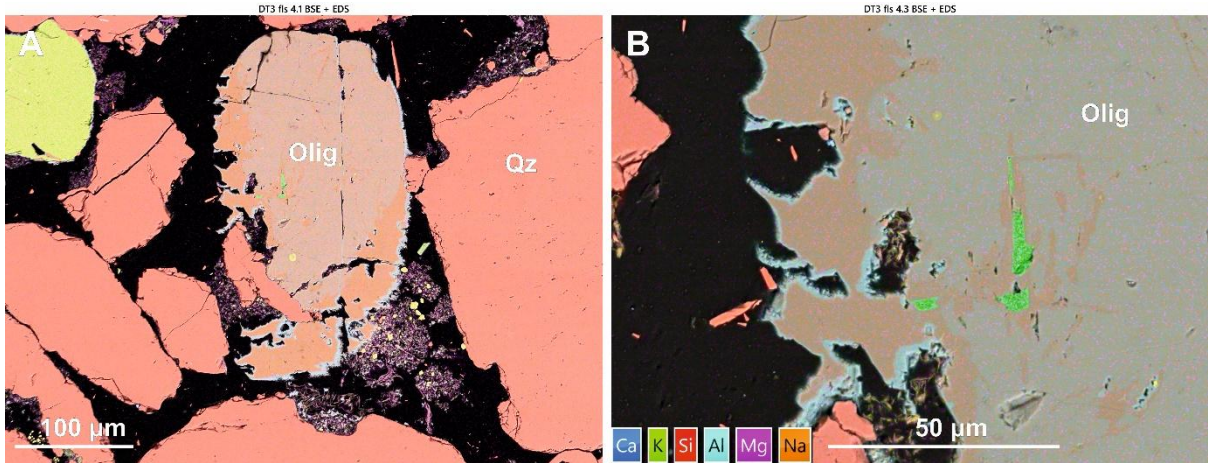
385
386 **Figure 8. Back scattered electron (BSE) images with overlain EDS map showing grain boundary dissolution**
387 **of oligoclase grains reacted with CO_2 fluids at 400°C.**

388 ### 3.2.2. *Plagioclase:H_2O pore fluids*

389 Experiments run with H_2O pore fluids show no obvious chemical alteration of albite or

390 oligoclase at experiments conducted at 400°C and below, but in these samples the oligoclase

391 grains do show more intergranular fractures with many grains fractured along cleavage planes

392 (Fig 9.a). At higher temperatures (550°C) some oligoclase grains show chemical dissolution

393 and 'scalloping' of the grain boundary (Supp. Mat, Fig 12) with few grains exhibit a thick,

394 porous texture calcite overgrowths apparently tracking the original grain boundary as this

395 boundary abuts the contact with quartz grains (Fig 9.e and f). In this sample calcite cements

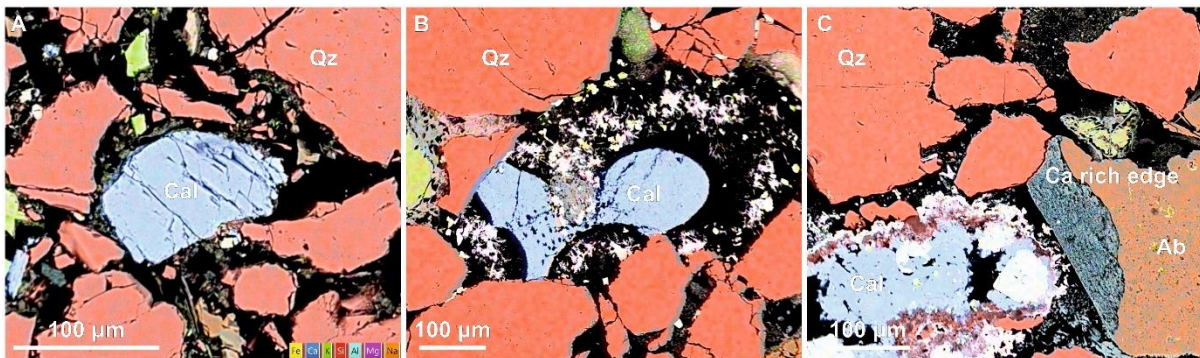396 are still present as singular, isolated patches of cement (Fig 10.c and Supp. Mat, Fig 13).

397
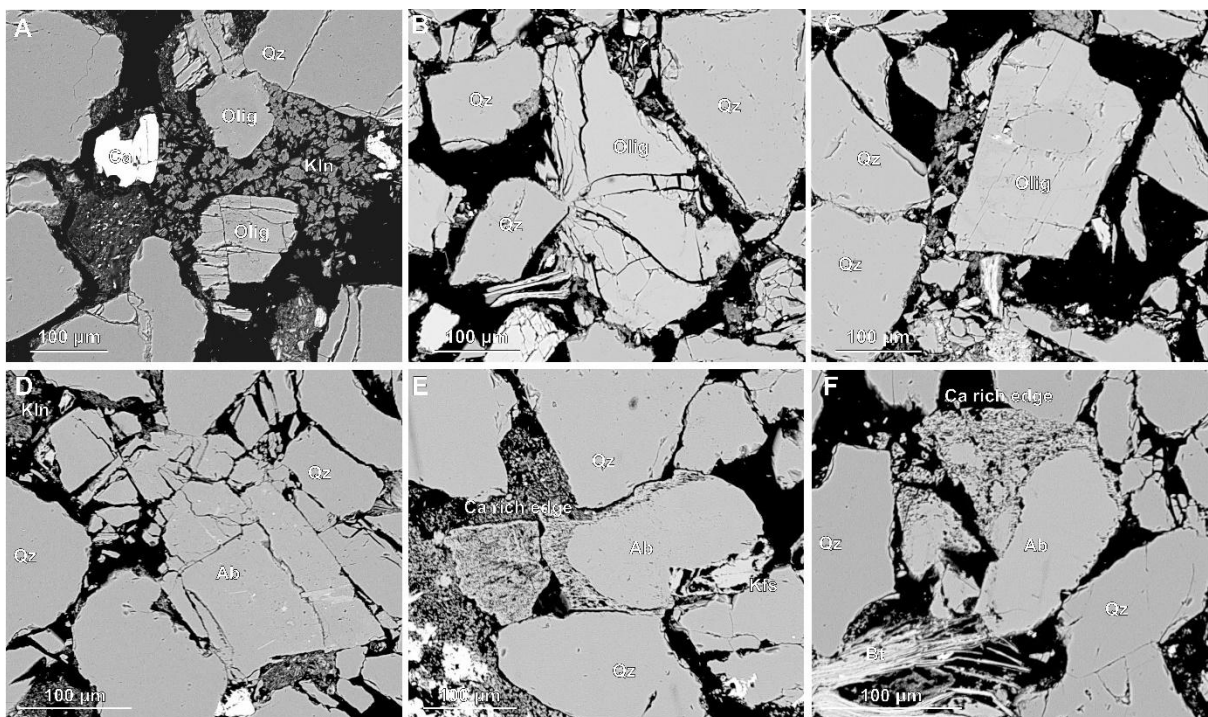
Figure 9. Backscattered electron (BSE) images of plagioclase feldspar grains (including both oligoclase and albite) following reaction with H_2O pore fluid. Images from 80°C and 250°C experiments (a–c) show enhanced mechanical fracturing with minimal evidence of chemical alteration. Albite reacted at 550°C (d) also displays fracturing without signs of chemical dissolution. In contrast oligoclase grains reacted at 550°C appear partially dissolved, with sodium leached from the grains, resulting in a calcite rich grain boundary presenting with a porous 'mesh' texture (e and f).

3.3. Dissolution of calcite grains and cement with CO_2 enriched water and H_2O pore fluids

Pre experiment samples recorded XRD analysis recorded around 1% calcite which occurred as both grains and cement (Supp. Mat, Fig 4). Following the experiments, calcite was nearly entirely removed in the CO_2 experiment samples, whereas it remained visible in post H_2O experiment samples (even at temperatures up to 550 °C) as grains and patches of cement (Figure 10).

Figure 10. Back scattered electron images of calcite grains and calcite cement in post H_2O experiment samples reacted at 250°C (a), 400°C (b), 550°C (c).

3.4. Quantitative microstructural and mineralogical alteration

Image analysis was performed to quantify mineral alteration in both CO_2 and H_2O experiment samples. Specifically, changes in the 2D percentage of pore area and the key reactive minerals (K-feldspar, plagioclase, and calcite) were measured. To account for heterogeneity and spatial distribution, the percentage area of each mineral was quantified from multiple subsections of each thin section (between six and twelve 3x3 mm images per sample) following methodology used in Hall et al (2015). The results are presented using box-and-whisker plots to illustrate the data spread and account for heterogeneity (Fig 11). Two pre-experiment samples, 'Dt' and 'Dm', were analysed, each with slightly different pre experiment bulk rock compositions (see Supp. Mat, Table 2). Core plugs from the Dm sample were primarily used in H_2O experiments, while Dt sample core plugs were used in CO_2 experiments.

Image analysis revealed minimal changes in 2D pore area between pre-experiment samples, which averaged 29% and 32% pore area and post-experiment reacted with H_2O and CO_2 at 80°C and 250°C, which averaged 30% and 32%) (Fig 11.a). However, this decreased to 26%

428   pore area in samples reacted with H_2O and CO_2 at 400°C and with H_2O 550°C, possibly due to

429   enhanced grain packing and pressure solution observed in images (Fig 9.e and Supp. Mat, Fig

430   11) and secondary mineral precipitation, while samples exposed to CO_2 at 550°C maintained

431   pore areas over 30% (Fig. 4.a). This difference is likely due to additional secondary porosity

432   produced by K-feldspar and calcite cement and grain dissolution (Supp. Mat, Fig 8) as pressure

433   solution and mineral precipitation are also observed in these samples (Fig 7.f and Supp. Mat,

434   Fig 7).

435   Boxplots show the percentage of reactive grains (K-feldspar, plagioclase, and calcite)

436   expressed as their proportion relative to the total number of mineral grains visible in each image

437   (Fig 11.b – d). The average proportion of K-feldspar grains decreased by nearly half in all

438   samples exposed to H_2O and CO_2, with a more significant reduction observed in post CO_2

439   experiment samples (Fig 11.b). These CO_2 reacted samples also exhibited a more

440   heterogeneous distribution of K-feldspar, as indicated by the wider interquartile ranges on the

441   grey CO_2 box-and-whisker plots compared to the blue H_2O boxes, suggesting variable

442   dissolution across the sample (Fig. 11.b). Due to limitations in image thresholding, albite and

443   oligoclase were grouped together under the category of 'all plagioclase'. In samples reacted

444   with CO_2, the proportion of plagioclase decreased by approximately 25%, indicating some

445   dissolution. In contrast, H_2O-reacted samples show little change in plagioclase area (Fig. 11c).

446   XRD analysis determined ~1% calcite in the pre-experiment samples (Supp. Mat, Table 1),

447   observed in thin sections as carbonate clasts, bioclasts, and carbonate cement patches (Supp.

448   Mat, Fig. 4). Quantitative image analysis showed low area fractions of calcite across many pre-

449   and post-experiment images (0–0.9%). Pre-experiment samples had median calcite area

450   fractions of 0.2% and 0.4%, whereas post-experiment samples generally showed lower median

451   values. In CO_2-reacted samples, calcite abundance decreased by more than half at 80 °C and

452   250 °C, with calcite nearly absent at 400 °C and 550 °C (Fig. 11d). In contrast, H_2O-reacted

453   samples showed only a slight decrease at 80 °C, with calcite contents remaining largely

454   unchanged at higher temperatures.
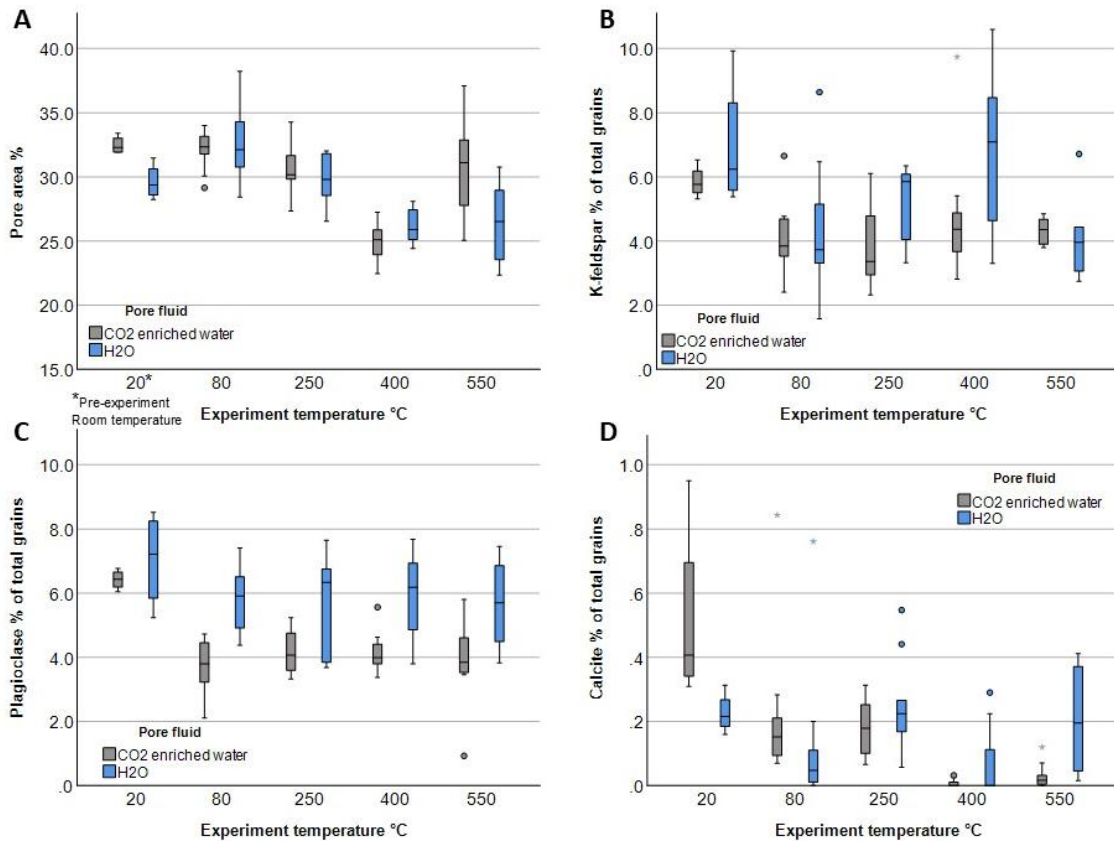
Figure 11. Box and whisker plots d in pore area and reactive mineral content in Captain Sandstone samples before and after reaction, experiments, based on thresholded EDS images. Two pre-reaction samples, 'Dt' and 'Dm', with slightly different bulk compositions were used: Dm cores (H_2O experiments) and Dt cores (CO_2 experiments), shown in grey and blue respectively. Box plots display data spread, including median, interquartile range (IQR), and outliers.

4. Discussion

4.1. Experimental reaction mechanisms and microstructural evolution

Microstructural analysis of reacted samples reveals a complex interplay of feldspar dissolution and secondary mineral precipitation in the presence of H_2O and CO_2-enriched pore fluids. These reactions are driven by deformation mechanisms such as diffusive mass transfer, including pressure solution, microfracturing, which generates fresh surfaces and increases reactivity, ion exchange and hydrolysis. Key contrasts between H_2O and CO_2 fluid experiments samples include: 1) early incongruent dissolution of K-feldspar in CO_2 experiments conducted at 80 °C, as CO_2-enriched fluids, weakened grains and promoted microfracturing; 2) extensive congruent dissolution K-feldspar in higher temperature >250°C experiments with CO_2, which resulted in grain size reduction, creation of secondary pores and increase in pore area; 3) near-

19

472 complete dissolution of calcite grains and cements in CO_2 experiments, compared to partial

473 dissolution with H_2O; and 4) partial dissolution and incongruent leaching of calcium from

474 oligoclase grains from 80 °C with CO_2, resulting in grain area reduction that was not observed

475 in H_2O experiments, (Figure 11). Reactions, deformation mechanisms observed in experiments

476 are summarised in Table 2 and key mineral phases present in the Cretaceous Captain sandstone

477 before, during and after experiments are highlighted in Figure 12.

4.1.1. Feldspar deformation and reaction textures

479 Our results show that at reservoir temperatures CO_2 enriched fluids created a chemically

480 reactive environment that promoted compositionally preferential, incongruent dissolution of

481 K-feldspar and oligoclase. In K-feldspar this produced parallel porous 'seams' that developed

482 on the edge of grains, possibly exploiting cleavage planes (Fig 5.a). These features were absent

483 in higher temperature experiments, possibly because 1) they represented early-stage dissolution

484 textures that were overprinted by later grain dissolution or 2) experiments at higher

485 temperatures (above 250°C) produced a shift in the dominant reaction mechanism from ion

486 exchange reactions (i.e. early incongruent release of K^+, Na^+, and Ca^{2+}) to hydrolysis-driven

487 dissolution (i.e. congruent breakdown of the Si-O framework). Similar temperature-dependent

488 dissolution styles have been observed in previous feldspar reaction experiments on microcline

489 (Fung et al., 1980), albite (Chen et al., 2000), and labradorite (Carroll and Knauss, 2005).

490 K-feldspars with incongruent dissolution textures produced at lower reservoir temperatures

491 appeared to be mechanically weaker and more susceptible to the effects of grain-to-grain

492 stresses under confining pressure, which led to microfracturing and crushing between the more

493 resistant quartz grains (Fig. 4; Supp. Mat. Figs. 5–7). In turn, these 'fresh' microfractures and

494 fragmented grains created more reactive surfaces, which drove further dissolution in a positive

495 feedback loop of 'incongruent dissolution, stress-induced microfracture, and enhanced grain

496 reactivity'. This process likely accelerated the significant K-feldspar comminution and

497 dissolution textures observed after higher temperature experiments.

498 In plagioclase, interaction with CO_2-enriched fluid had no apparent effect on albite grains but

499 oligoclase showed partial dissolution, evident as wavy grain boundaries and localised

500 compositional zoning (Fig 8). EDS analysis indicated that this texture was formed by

501 incongruent dissolution, with calcium being selectively leached from the edge of grains leaving

502 a sodium rich outer zone around an intact Ca-Na rich grain centre (Fig 8). A thin Ca-rich rim

503 at the grain edge was also observed. While grain weakening evidenced by microfracturing was

504   less evident in altered oligoclase grains, pressure solution features (e.g., concave–convex
505   contacts) suggests stress-driven mass transfer played a role in the evolution of these dissolution
506   textures.

4.1.2. Coupled dissolution-precipitation and ion exchange

508   At >400°C in both H_2O and CO_2 experiments, K-feldspar dissolution was coupled with
509   secondary mineral precipitation. This included pore-filling masses, overgrowths and fracture
510   fills of calcic aluminosilicate rims and K-bearing clays associated with dissolving K-feldspar
511   grains (Fig 5.d and Supp Mat., Fig 14). Despite the sharp boundary between the primary K-
512   feldspar and secondary calcic aluminosilicates, optical continuity between secondary phases
513   and host grains indicates epitaxial growth via ion exchange as Ca^{2+} in the pore fluid was
514   substituted for K^+ in K-feldspar. Quantitative surface area analysis showed K-feldspar and
515   calcite as dominant dissolving phases in H_2O and CO_2 experiments (Fig 11). While incongruent
516   dissolution of oligoclase in CO2 experiments contributed additional Ca^{2+} via leaching (Fig. 8).
517   The resulting enrichment likely induced supersaturation, triggering precipitation of calcic
518   aluminosilicates and potassic aluminosilicates (K-clays) (Fig 5).

519   Similar coupled dissolution-precipitation (CDP) reactions in K-feldspar have previously been
520   observed both in nature (Cole et al., 2004, Moore et al, 2005; Baines and Worden; 2004) and
521   experiments (Putnis et al., 2007b; Niedermeier et al, 2009; Norberg et al., 2011; Abart et al.,
522   2012). For example, albitisation of sanidine and orthoclase by Na-Cl fluids via CDP produced
523   sharp reaction interfaces with crystallographically aligned albite overgrowths (Norberg et al.,
524   2011). In another experimental study, the replacement of albite by K-feldspar produced sharply
525   defined reaction fronts while preserving the crystallographic orientation of the host grain
526   (Niedermeier et al., 2009). Additionally, similar to the parallel dissolution seams observed in
527   our study, Niedermeier reported aligned 'tubular nanopores' normal to the replacement interface
528   which they interpreted as pathways for fluid access to the reaction front (Niedermeier et al.,
529   2009). Such nanotube formation appears to be a common feature of reaction fronts in mineral
530   lattices (Harlov et al., 2005; Zeitler et al., (2017).

4.1.3. Anorthitisation of K-feldspar comparison to previous studies

532   In this study, we observed the replacement of K-feldspar by calcic aluminosilicates i.e.
533   'anorthitisation', under experimental conditions (400°C, 70MPa confining pressure).
534   Anorthitisation has been described in natural systems, e.g. the transformation of andesine to

535 anorthite in the presence of Ca^{2+}-rich meteoric fluids (Mora et al., 2009) and has been described

536 conceptually in the framework of CDP reactions (Putnis, 2009). Though K-feldspar alteration

537 via direct K^+- Ca^{2+} substitution has not been described previously in geological settings, there

538 are natural examples of K-feldspar alteration involving Ca-bearing fluids. These include high

539 temperature hydrothermal systems where K-feldspar is replaced by Na-Ca plagioclase and

540 myrmekite textures form via K, Na, and Ca exchange (Chakrabarty et al., 2023). And low

541 temperature settings in CO_2-rich basins like Otway and Bravo Dome where fluid acidification

542 drives feldspar dissolution and precipitation of Ca-bearing phases such as dawsonite and calcic

543 zeolites, (Mora et al., 2009; Wigley et al., 2013; Baines and Worden, 2004).

544 While the replacement of K-feldspar by calcic aluminosilicates via ion exchange has not been

545 previously described under controlled laboratory conditions in geoscience, it has been explored

546 and established in materials science. Specifically, anorthitisation via ion exchange is being

547 investigated as a method for extracting potassium from K-feldspar using calcium-bearing fluids

548 as an alternative method for fertiliser production. Although not yet commercially implemented,

549 laboratory studies have shown K^+ leaching from K-feldspar powders at temperatures as low as

550 65°C (Ma et al., 2016; Ciceri et al., 2017), and the formation of calcic aluminosilicate phases,

551 texturally similar to those observed in our experiments, at 160 °C (Liu et al., 2015; Yuanyuan

552 et al., 2020; Haseli et al., 2020; Zhai et al., 2021). These findings suggest that ion exchange via

553 CDP observed in our study may represent a previously unrecognised mechanism for K-feldspar

554 alteration in the presence of CO_2-enriched fluids.

555

556

| Experiment temperature (°C)	K-feldspar		Oligoclase		Albite	
	Chemical alteration	Mechanical deformation	Chemical alteration	Mechanical deformation	Chemical alteration	Mechanical deformation
80	Localised **incongruent dissolution** producing grain-edge, cleavage-parallel porous seams; preferential release of K^+ ($\pm Na^+$, Ca^{2+})	Stress-assisted **microfracturing** and local grain crushing against quartz, enhanced by chemical weakening	**Incongruent dissolution** around grain boundary with early Ca^{2+} leaching creating scalloped edges	Grains largely intact with no microfracturing	Largely unaltered; skeletal textures preserved	Coherent, no microfracturing
250	Transition toward more **congruent dissolution** along microfractures, increasing reactive surface area	Intergranular **microfracturing** generating fresh reactive surfaces	Continued **incongruent dissolution producing** some intergranualar porosity and indented grain boundaries rimmed by kaolinite and mixed clays	Minor deformation with compaction and minor **microfracturing**	Largely unaltered	Coherent, no microfracturing
400	Coupled dissolution–precipitation (CDP) reaction during K-feldspar dissolution and precipitation of thin (~3 µm) calcic aluminosilicate rims and K-bearing clays via ion exchange (K^+–Ca^{2+})	Sets of through-going, **cross-cutting microfractures** possibly aligned along cleavage and/or chemically altered grain	**Dissolution** increases intergranular porosity by **leaching** of Ca^{2+} from edges leaving 20–30 µm Na-rich boundary and thin 2–5 µm Ca-rich rim	Limited **microfracturing,** fractures less pervasive than K-feldspar	Minimal chemical change	Coherent, skeletal textures maintained
550	Extensive congruent dissolution and grain comminution producing significant secondary porosity. Precipitation of thick (~10 µm) calcic aluminosilicate (anorthitisation) and K-clays	Concave–convex grain contacts with quartz indicating **pressure solution**	Continued **dissolution** and **precipitation** developing albitic rims and enhancing intergranular porosity	Minor **pressure solution** features at grain contacts	Largely unaltered	Coherent, skeletal textures maintained

557
558 **Table 2. Summary of observed chemical and mechanical alteration and interpreted reactions and deformation mechanisms from experiments reacting CO2 enriched**
559 **fluids with core plugs of Cretaceous Captain Sandstone 'D sand' from the Acorn CCS field.**
560

4.1.4. Source of calcium

In natural systems, Ca^{2+} is typically derived from hydrothermal fluids or CO_2-enriched waters that leach calcium from carbonates, plagioclase, or mafic phases. In our experiments, elevated calcium in the pore fluid resulted from 1) dissolution of calcite grains and cement, prominent in all CO_2 experiments, and to a lesser degree in H_2O experiments >400°C, and 2) partial dissolution of oligoclase, observed only in CO_2 experiments. Incongruent dissolution of plagioclase is well established, for example, a previous experimental study on labradorite showed that calcium release rates exceeded silica release by a factor of three, highlighting strongly incongruent behaviour (Knauss and Wolery, 1988). This likely explains why we observed preferential calcium leaching from oligoclase, producing a Na-rich rim around an intact Na-Ca grain core. The precipitation of secondary calcic aluminosilicate phases may have further contributed to calcium leaching, as the removal of Ca^{2+} from the pore fluid enhanced chemical disequilibrium and promoted continued oligoclase dissolution.

Previous studies on the Captain Sandstone 'D sand' also observed calcite dissolution during CO_2 flow-through experiments at <60 °C (Hangx et al., 2013). However, this study focused on the effect of calcite dissolution on rock mechanical strength and, although they also noted K-feldspar dissolution, did not examine the coupled mechanisms driving geochemical alteration or potential for ion exchange.
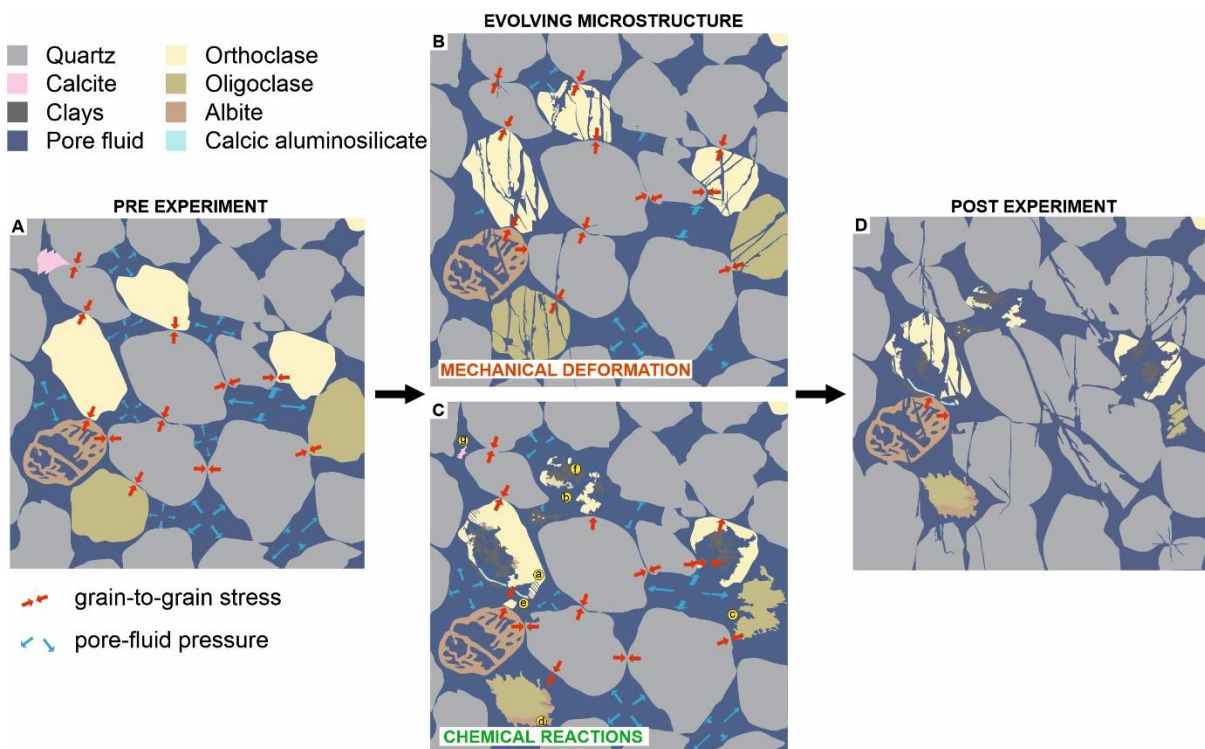
Figure 12. Schematic summary of the coupled mechanical and chemical changes identified from hydrostatic batch experiments using CO$_2$-enriched pore fluids on the Captain Sandstone ('D sand'). Experiments were conducted at reservoir-relevant confining and pore fluid pressures, generating grain to grain scale stresses at temperatures of 80–550 °C. These conditions promote interacting mechanical and chemical feedbacks that drive the evolution of sandstone microstructure and texture. (A) Pre-experimental sandstone texture with intact K-feldspar (orthoclase), calcic plagioclase (oligoclase), skeletal albite, and minor calcite cement (B) Mechanical deformation preferentially fractures feldspars relative to quartz, creating fresh reactive surfaces and increasing feldspar–fluid contact. (C) Chemical reactions include (a) orthoclase dissolution expressed as parallel cracks penetrating from grain margins to interiors, (b) orthoclase grain dissolution, (c) oligoclase dissolution, (d) albitisation of oligoclase, (e) precipitation of calcic aluminosilicate, (f) precipitation of clay minerals (muscovite–illite), and (g) dissolution of calcite cement. (D) Post-experiment analysis illustrates how coupled deformation–dissolution and new mineral precipitation reshape the microstructure.

4.1.5. Role of stress

Although our experiments were successfully designed to limit mechanical compaction (confirmed by maintenance of pore area in H$_2$O and CO$_2$ runs up to 250 °C), features indicative of chemical compaction via pressure solution, such as concave–convex grain contacts, were observed in both H$_2$O and CO$_2$ experiments above 400 °C. These suggest localised, stress-assisted dissolution at grain contacts under high temperature aka faster reaction rate experiments. This dissolution likely increased local K$^+$ concentration, providing micro-zones of supersaturation and promoting precipitation in adjacent lower-stress areas around grain boundaries. Analogous features are seen in natural CO$_2$ reservoirs like the Supai Sandstone Formation, where dawsonite precipitates are spatially associated with corroded K-feldspar and in the Triassic Chaunoy Formation, which associates feldspar dissolution textures with carbonate and zeolite formation (Moore et al., 2005; Baines and Worden, 2004 respectively).

4.2. Comparison to previous studies on CO$_2$:sandstone interaction

The enhanced dissolution of K-feldspar and calcite in CO$_2$-enriched fluids observed in our study aligns with previous experimental studies. For instance, a three-month CO$_2$ flow-through experiment at 140 °C resulted in K-feldspar dissolution, grain size reduction, and secondary porosity, leading to a 20% increase in porosity and increased permeability (Hall et al., 2015). Although no secondary precipitation occurred due to constant undersaturation, deformation textures e.g. altered feldspars and secondary porosity, closely resemble observations from our experiments. In addition to the dissolution of calcite cement noted in the Hangx study described above, carbonate mineral dissolution in sandstones reacted with CO$_2$-enriched fluids is

experimentally well established. Several studies have shown increased calcium concentrations in pore fluids following saturation of sandstone samples with CO_2 -enriched brines, many accompanied by a corresponding permeability increase (Ross et al., 1982; Sayegh et al., 1990; Hall, 2015; Foroutan, 2021). Precipitation of secondary phases was apparently not a limiting factor for K-feldspar dissolution in our experiments, contrasting with the experimental results of Lu et al, (2013), possibly due to fracture-induced increases in feldspar-fluid surface area.

Studies on feldspar alteration in geological CO_2-injection projects and natural CO_2 reservoirs also support our findings. In a study on the microstructural impact of CO_2 on sandstone in an engineered subsurface setting, the microstructure of pre- and post-core CO_2 flood sandstones from the Pembina Cardium CO_2 Monitoring Project in Canada showed partial dissolution of K-feldspar grains after two years of CO_2 injection (Nightingale et al., 2009). And as previously noted, natural CO_2 reservoirs such as Bravo Dome also show feldspar alteration and secondary mineral formation linked to long-term CO_2 exposure (Wigley et al., 2012). These findings confirm that feldspar alteration and associated secondary porosity development can occur over relatively short timescales in the subsurface and are comparable in character to the features we have observed in our higher-temperature experimental system.

4.3. Implications for CCS reservoirs

Our findings have several *direct* implications for geological storage of CO_2. Firstly, they demonstrate that K-feldspar and oligoclase in CO_2-enriched fluids at reservoir-relevant conditions can undergo rapid alteration including grain microcracking, dissolution and the development of secondary porosity. Second, they show that dissolution of even small amounts (e.g. 1%) of calcite grains and cement or leaching of calcium from plagioclase can elevate Ca^{2+} concentrations in the pore fluid and, depending on local fluid composition and saturation states, promote ion exchange with K-feldspar and drive the precipitation of calcic aluminosilicates and K-bearing clays. Third, the presence of pressure solution textures suggests that local stress concentrations create grain-scale chemical disequilibria, enhancing feldspar dissolution and promoting localised mineral precipitation, processes that are often overlooked in geochemical models of CCS systems.

These microstructural alterations have important implications for reservoir integrity and CCS project performance. Fracturing and dissolution of framework feldspars (~16 % of the D Sand) could reduce compressive strength, alter elastic properties, and modify porosity. These properties are key parameters in both geomechanical and fluid flow models and could alter the

646 predicted reservoir behaviour. Such changes would be especially critical near structural
647 features like faults, where shifts in strength or porosity may alter fault stability during fluid
648 injection/depletion. While the relatively unfaulted Acorn CCS site may be less susceptible to
649 fault reactivation, microstructural changes such as feldspar fracturing and dissolution could
650 still lead to mechanical compaction and reservoir fracturing. The impact of this may affect the
651 ability to flow CO_2 fluids into the reservoir, i.e. productivity. However, in some cases, such as
652 the Ekofisk field, reservoir collapse and compaction have paradoxically enhanced permeability
653 and improved production (Teufel, 1996).

654 Secondary mineral precipitation, such as K-bearing illite, could reduce permeability and hinder
655 CO_2 injection/migration, but feldspar dissolution, especially of Ca-bearing phases like
656 oligoclase may enhance long-term CO_2 sequestration by releasing Ca^{2+}. that can become
657 incorporated into secondary phases, possibly even locking in carbon. However, if Ca^{2+} instead
658 bonds with dissolving K-feldspar, it may reduce carbonate formation and limit carbon trapping
659 through mineralisation. Dawsonite did not form in our experiments, likely due to the low Na
660 and Cl content of our fluids. In natural CCS settings, brine compositions with higher Na
661 concentrations could promote dawsonite or other Na-bearing phase formation via K-feldspar
662 replacement. Instead, we observed formation of a calcic aluminosilicate, although we cannot
663 confirm whether it contained carbon, as our carbon-coated thin sections compromised EDS
664 detection.

665 *4.4. Experimental limitations*

666 While our findings offer empirical evidence for feldspar reactivity in CO_2-enriched fluids,
667 several limitations are acknowledged. Most notably, the elevated temperatures used in some
668 experiments accelerated reaction kinetics beyond those typical of natural systems. However,
669 the occurrence of similar dissolution reactions, albeit to a lesser extent, at reservoir
670 temperatures supports the relevance of our results to CCS reservoir and a comparison to
671 reaction rates on a geological timescale has been calculated (Supp Mat). Post-quench
672 precipitation of secondary phases cannot be ruled out, although the presence of well-
673 crystallised calcic aluminosilicate in optical continuity with host grains strongly suggest that
674 these minerals formed in situ during the experiments. This interpretation is consistent with
675 previous work which noted similar limitations and applied the same criteria to distinguish in-
676 experiment from post experiment precipitation (Rosenqvist et al., 2001).

677 For this study, we employed batch reactor experiments because they allow direct comparison

678 with the geochemical models used in the Acorn CCS Project (Shell, 2015. Batch systems are

679 optimal for studying both dissolution and precipitation processes as they more closely mimic

680 the generally static fluid conditions in subsurface reservoirs than flow through setups.

681 However, batch reactors do not simulate the effects of fluid flow, which in a CCS reservoir

682 would significantly influence reaction kinetics as the dissolved phases would be transported,

683 both reducing supersaturation and making for a dynamic ongoing pore fluid chemistry. As

684 previous CO_2:sandstone flow-through experiments have shown, undersaturation of the fluid

685 suppresses precipitation but enhances feldspar dissolution (Hall et al, 2015). For understanding

686 the interplay between reaction rate and transport in dynamic subsurface environments like CCS

687 reservoirs, both experimental styles are important. Another limitation is the use of tap water

688 rather than brine. Although selected to avoid the overly reactive behaviour of deionised water,

689 our fluid lacks the high Na^+ and Cl^- content typical of formation waters, which may influence

690 both dissolution and secondary mineral precipitation. Future work should incorporate brine

691 compositions and use flow-through systems under triaxial stress to better simulate reservoir

692 conditions.

693 Despite these limitations, our results provide some of the first experimental evidence for CO_2

694 fluid induced K-feldspar alteration under controlled conditions relevant to CCS subsurface

695 settings. This supports the idea that K^+–Ca^{2+} exchange can occur via coupled dissolution–

696 precipitation mechanisms, with implications for feldspar reactivity, reservoir evolution, and

697 long-term mineral trapping in CCS scenarios.

698 **5. Summary**

699 This study offers new insights into mineral transformations and grain-scale deformation in a

700 planned CCS reservoir - processes that have been previously recognised in CO_2:sandstone

701 studies but never systematically investigated. This study also provides the first geological

702 evidence that Ca^{2+} released from experimental dissolution of detrital feldspar grains in a

703 sandstone (i.e. not freshly ground-up powder) can drive in-situ K^+ - Ca^{2+} ion exchange in K-

704 feldspar under realistic subsurface conditions.

705 Consistent with our hypothesis, experimental results showed that:

706 1) K-feldspar is more reactive than expected when exposed to disequilibrium fluids (both H_2O

707 and CO_2) under subsurface hydrostatic stresses at temperature; and

708   2) in comparison to H_2O, CO_2-enriched fluids significantly altered solubility of both

709   plagioclase and K-feldspar and produced distinct microstructural changes even during short (6-

710   day) experiments.

711   At reservoir temperatures (80 °C), CO_2-enriched fluids induced incongruent dissolution and

712   deformation of K-feldspar and dissolution of detrital calcite via ion exchange underscoring the

713   relevance of these transformations to CCS settings. At higher temperatures, where reaction

714   kinetics were accelerated, both H_2O and CO_2 fluids promoted dissolution of reactive minerals

715   - K-feldspar, oligoclase, and calcite - leading to the precipitation of secondary aluminosilicate

716   and clay phases. We propose that these transformations reflect a coupled dissolution–

717   precipitation mechanism, where Ca^{2+} released from calcite and oligoclase dissolution activates

718   and sustains K-feldspar alteration and subsequent dissolution. Crucially, the formation of

719   epitaxial Ca-bearing overgrowths on K-feldspar grains provides clear experimental evidence

720   for K^+ - Ca^{2+} ion exchange. While this anorthitisation of K-feldspar has been engineered in

721   materials science studies using Ca-rich fluids, this study is the first to demonstrate the reaction

722   occurring *in situ*—i.e., within intact rock, under subsurface stress using weakly CO_2-enriched

723   fluids.

724   As discussed, previous experimental and natural studies show that feldspar alteration can

725   involve coupled dissolution, ion exchange, and secondary mineral formation. Our findings

726   build on this by demonstrating more varied modes of feldspar transformation with CO_2-

727   enriched and calcium bearing fluids. While consistent with earlier CO_2- sandstone work, this

728   study uniquely combines microstructural and geochemical changes created under known

729   conditions to map possible reaction pathways and quantify the impact on mineral texture and

730   microstructure. These processes, often difficult to capture in reactive transport models, could

731   significantly affect reservoir properties like pore volume, fluid flow, and geomechanical

732   integrity.

733   *5.1. Outlook on remaining challenges*

734   Chemical mapping and compositional analyses suggest that feldspar zoning may influence

735   dissolution behaviour, although further investigation is required. The original chemical

736   homogeneity of the feldspars and their provenance appear to be important factors controlling

737   reactivity, which could have implications for other arkosic reservoir systems. More broadly,

738   this study raises new questions about the timing and mechanisms of feldspar reactivity in

739   stressed, fluid-saturated environments. It demonstrates the need to reconsider CCS appraisal

740   approaches, which often assess geochemical and geomechanical behaviour separately. Our

741   findings support a more integrated understanding of these processes and have wider relevance

742   for other subsurface applications, including geothermal energy and mineral extraction. Finally,

743   quantifying feldspar dissolution kinetics remains a key challenge due to the formation of

744   secondary clays and interactions with other phases. Future work should focus on simplified,

745   monomineralic synthetic systems with controlled textures and grain sizes to isolate, and thereby

746   better constrain, reaction rates.

747   **Author contribution**: Design of this project and acquisition of funding were carried out by

748   Natalie Farrell, Michael Flowerdew, and Kevin Taylor. Natalie Farrell designed the

749   experiments and prepared samples, and PDRA's Lining Yang and Nico Bigaroni carried them

750   out. Lee Paul provided technical support i.e. tooling, fixing the rig pump. Michael Flowerdew

751   and Lewis Hughes collected SEM BSE and EDS images. Natalie Farrell, Michael Flowerdew,

752   Chris Mark and Michael Pointon conducted analysis of microstructural and geochemical data.

753   Buhari Ardo and Kevin Taylor collected XCT data and processed and analysed the images.

754   John Waters carried out XRD analysis. Natalie Farrell prepared the manuscript with

755   contributions from all co-authors.

764   **References**

765   Alcalde, J., Heinemann, N., Mabon, L., Worden, R.H., De Coninck, H., Robertson, H.,

766   Maver, M., Ghanbari, S., Swennenhuis, F., Mann, I. & Walker, T. *Acorn: Developing*

767   *full-chain industrial carbon capture and storage in a resource- and infrastructure-rich*

768   *hydrocarbon province*. Journal of Cleaner Production, 233, pp. 963–971.

769   https://doi.org/10.1016/j.jclepro.2019.06.087, 2019.

770   Baines, S. J. and Worden, R. H.: The long-term fate of CO_2 in the subsurface: natural

771   analogues for CO_2 storage, in: **Geological Storage of Carbon Dioxide**, Geological Society

772   Special Publication 233, edited by: Baines, S. J. and Worden, R. H., Geological Society,

773   London, UK, 59–85, https://doi.org/10.1144/GSL.SP.2004.233.01.06, 2004.

774   Benson, S.M. and Cole, D.R. CO2 sequestration in deep sedimentary

775   formations. *Elements*, *4*(5), pp.325-331. https://doi.org/10.2113/gselements.4.5.325, 2008.

776   Bertier, P., Swennen, R., Laenen, B., Lagrou, D. and Dreesen, R. Experimental identification

777   of CO2–water–rock interactions caused by sequestration of CO2 in Westphalian and

778   Buntsandstein sandstones of the Campine Basin (NE-Belgium). *Journal of geochemical*

779   *exploration*, *89*(1-3), pp.10-14. https://doi.org/10.1016/j.gexplo.2005.11.005, 2006.

780   Blum, A. E. and Stillings, L. L.: Feldspar dissolution kinetics, in: Chemical Weathering Rates

781   of Silicate Minerals, Reviews in Mineralogy, Vol. 31, edited by: Brantley, S. L., American

782   Mineralogical Society, Washington, DC, USA, 291–351,

783   https://doi.org/10.1515/9781501509650-009, 1995.

784   Carroll, S.A. and Knauss, K.G. Dependence of labradorite dissolution kinetics on CO2 (aq),

785   Al (aq), and temperature. *Chemical Geology*, *217*(3-4), pp.213-225.

786   https://doi.org/10.1016/j.chemgeo.2004.12.008, 2005.

787   Putnis, C.V., Geisler, T., Schmid-Beurmann, P., Stephan, T. and Giampaolo, C. An

788   experimental study of the replacement of leucite by analcime. *American Mineralogist*, *92*(1),

789   pp.19-26. https://doi.org/10.2138/am.2007.2249, 2007.

790   Chakrabarty, A., Mukherjee, S., Karmakar, S., Sanyal, S. and Sengupta, P. Petrogenesis and

791   in situ U-Pb zircon dates of a suite of granitoid in the northern part of the Central Indian

792   tectonic Zone: Implications for prolonged arc magmatism during the formation of the

793   Columbia supercontinent. *Precambrian Research*, *387*, p.106990.

794   https://doi.org/10.1016/j.precamres.2023.106990, 2023.

795   Chen, Y., Brantley, S.L. and Ilton, E.S. X-ray photoelectron spectroscopic measurement of the

796   temperature dependence of leaching of cations from the albite surface. *Chemical*

797   *Geology*, *163*(1-4), pp.115-128. https://doi.org/10.1016/S0009-2541(99)00096-0, 2000.

798   Ciceri, D., de Oliveira, M. and Allanore, A. Potassium fertilizer via hydrothermal alteration of

799   K-feldspar ore. *Green Chemistry*, *19*(21), pp.5187-5202.

800   https://doi.org/10.1039/C7GC02633A, 2017.

801 Cole, D.R., Larson, P.B., Riciputi, L.R. and Mora, C.I. Oxygen isotope zoning profiles in
802 hydrothermally altered feldspars: Estimating the duration of water-rock
803 interaction. *Geology*, *32*(1), pp.29-32. https://doi.org/10.1130/G19881.1, 2004.

804 Collettini, C., Tesei, T., Scuderi, M.M., Carpenter, B.M. and Viti, C. Beyond Byerlee friction,
805 weak faults and implications for slip behavior. *Earth and Planetary Science Letters*, *519*,
806 pp.245-263. https://doi.org/10.1016/j.epsl.2019.05.011, 2019.

807 Correns, C.W. February. Experiments on the decomposition of silicates and discussion of
808 chemical weathering. In *Clays and Clay Minerals (National Conference on Clays and Clay
809 Minerals)* (Vol. 10, pp. 443-459). Cambridge University Press & Assessment.
810 https://doi.org/10.1346/CCMN.1961.0100139, 1961.

811 Dove, P.M. and Crerar, D.A. Kinetics of quartz dissolution in electrolyte solutions using a
812 hydrothermal mixed flow reactor. *Geochimica et cosmochimica acta*, *54*(4), pp.955-969.
813 https://doi.org/10.1016/0016-7037(90)90431-J, 1990.

814 Durst, P. and Vuataz, F. D.: Fluid-rock interactions in hot dry rock reservoirs: a review of the
815 HDR sites and detailed investigations of the Soultz-sous-Forêts system, in: *Proceedings of the
816 World Geothermal Congress 2000*, World Geothermal Congress, Kyushu–Tohoku, Japan, June
817 2000, 3677–3682, no DOI available, 2000.

818 Farrell, N.J.C. and Healy, D. Anisotropic pore fabrics in faulted porous sandstones. *Journal of
819 Structural Geology*, *104*, pp.125-141. https://doi.org/10.1016/j.jsg.2017.09.010, 2017.

820 Farrell, N.J.C., Debenham, N., Wilson, L., Wilson, M.J., Healy, D., King, R.C., Holford, S.P.
821 and Taylor, C.W., 2021. The effect of authigenic clays on fault zone permeability. *Journal of
822 Geophysical Research: Solid Earth*, *126*(10), https://doi.org/10.1029/2021JB022615, 2021.

823 Flowerdew, M. J., Farrell, N., Yang, L., Badenszki, E., Mark, C., Ardo, B., and Taylor, K.:
824 Feldspars in CCS reservoirs: overlooked or unimportant?, in: *CCS4G Symposium 2024*,
825 CCS4G Symposium, London, UK, 17 December 2024, 2024, no DOI available. 2024.

826 Folk, R.L., Andrews, P.B. and Lewis, D.W. Detrital sedimentary rock classification and
827 nomenclature for use in New Zealand. *New Zealand journal of geology and geophysics*, *13*(4),
828 pp.937-968. https://doi.org/10.1080/00288306.1970.10418211, 1970.

829 Foroutan, M., Ghazanfari, E. and Amirlatifi, A. Variation of failure properties, creep response
830 and ultrasonic velocities of sandstone upon injecting CO2-enriched brine. *Geomechanics and*

831   *Geophysics for Geo-Energy and Geo-Resources*, *7*(2), p.27. https://doi.org/10.1007/s40948-
832   021-00223-y, 2021.

833   Fuchs, S.J., Espinoza, D.N., Lopano, C.L., Akono, A.T. and Werth, C.J. Geochemical and
834   geomechanical alteration of siliciclastic reservoir rock by supercritical CO2-saturated brine
835   formed during geological carbon sequestration. *International Journal of Greenhouse Gas*
836   *Control*, *88*, pp.251-260. https://doi.org/10.1016/j.ijggc.2019.06.014. 2019.

837   Fung, P.C., Bird, G.W., McIntyre, N.S., Sanipelli, G.G. and Lopata, V.J. Aspects of feldspar
838   dissolution. *Nuclear technology*, *51*(2), pp.188-196. https://doi.org/10.13182/NT80-A32600,
839   1980.

840   Glasmann, J.R. The fate of feldspar in Brent Group reservoirs, North Sea: A regional synthesis
841   of diagenesis in shallow, intermediate, and deep burial environments. *Geological Society,*
842   *London,*   *Special*   *Publications*, *61*(1),   pp.329-350.
843   https://doi.org/10.1144/GSL.SP.1992.061.01.17. 1992.

844   Hall, M.R., Dim, P.E., Bateman, K., Rochelle, C.A. and Rigby, S.P. Post-CO2 injection
845   alteration of pore network geometry and intrinsic permeability of Permo Triassic sandstone
846   reservoir". Geofluids, doi:10.1111/gfl. 12146, 2015.

847   Hangx, S., Bakker, E., Bertier, P., Nover, G. and Busch, A. Chemical–mechanical coupling
848   observed for depleted oil reservoirs subjected to long-term CO2-exposure–A case study of the
849   Werkendam natural CO2 analogue field. *Earth and Planetary Science Letters*, *428*, pp.230-
850   242. https://doi.org/10.1016/j.epsl.2015.07.044, 2015.

851   Harlov, D.E., Wirth, R. and Förster, H.J., 2005. An experimental study of dissolution–
852   repreciptation in fluorapatite: fluid infiltration and the formation of monazite. *Contributions*
853   *to Mineralogy and Petrology*, *150*(3), pp.268-286. https://doi.org/10.1007/s00410-005-0017-
854   8, 2005.

855   Haseli, P., Majewski, P., Christo, F., Raven, M., Klose, S. and Bruno, F. Experimental kinetic
856   analysis of potassium extraction from ultrapotassic syenite using NaCl–CaCl2 salt mixture. *Acs*
857   *Omega*, *5*(27), pp.16421-16429. https://doi.org/10.1021/acsomega.0c00549, 2020.

858   Helgeson, H.C., Murphy, W.M. and Aagaard, P. Thermodzhuynamic and kinetic constraints
859   on reaction rates among minerals and aqueous solutions. II. Rate constants, effective surface
860   area, and the hydrolysis of feldspar. *Geochimica et Cosmochimica Acta*, *48*(12), pp.2405-2432.
861   https://doi.org/10.1016/0016-7037(84)90294-1, 1984.

862   Hellmann, R., Wirth, R., Daval, D., Barnes, J.P., Penisson, J.M., Tisserand, D., Epicier, T.,
863   Florin, B. and Hervig, R.L. Unifying natural and laboratory chemical weathering with
864   interfacial dissolution–reprecipitation: a study based on the nanometer-scale chemistry of
865   fluid–silicate interfaces. *Chemical Geology*, *294*, pp.203-216.
866   https://doi.org/10.1016/j.chemgeo.2011.12.002, 2012.

867   IPCC: Special Report on Carbon Dioxide Capture and Storage, Cambridge University Press,
868   Cambridge, 431 pp., 2005.

869   Juanes, R., Spiteri, E.J., Orr Jr, F.M. and Blunt, M.J. Impact of relative permeability hysteresis
870   on geological CO_2 storage. *Water resources research*, *42*(12).
871   https://doi.org/10.1029/2005WR004806, 2006.

872   Knauss, K.G. and Wolery, T.J. Dependence of albite dissolution kinetics on pH and time at 25
873   C and 70 C. *Geochimica et Cosmochimica Acta*, *50*(11), pp.2481-2497.
874   https://doi.org/10.1016/0016-7037(86)90031-1, 1986.

875   Liu, S.K., Han, C., Liu, J.M. and Li, H. Hydrothermal decomposition of potassium feldspar
876   under alkaline conditions. *Rsc Advances*, *5*(113), pp.93301-93309.
877   https://doi.org/10.1039/C5RA17212H. 2015.

878   Lu, P., Fu, Q., Seyfried Jr, W. E., Hedges, S. W., Soong, Y., Jones, K., Zhu, C. Coupled
879   alkali feldspar dissolution and secondary mineral precipitation in batch systems–2: New
880   experiments with supercritical CO_2 and implications for carbon sequestration. Appl.
881   Geochem. 30, 75–90. https://doi.org/10.1016/j.apgeochem.2012.04.005, 2013.

882   Ma, X., Ma, H. and Yang, J. Sintering preparation and release properties of $K_2MgSi_3O_8$ slow-
883   release fertilizer using biotite acid-leaching residues as silicon source. *Industrial &*
884   *Engineering Chemistry Research*, *55*(41), pp.10926-10931.
885   https://doi.org/10.1021/acs.iecr.6b02991, 2016.

886   Moore, J., Adams, M., Allis, R., Lutz, S. and Rauzi, S. Mineralogical and geochemical
887   consequences of the long-term presence of CO_2 in natural reservoirs: an example from the
888   Springerville–St. Johns Field, Arizona, and New Mexico, USA. *Chemical geology*, *217*(3-4),
889   pp.365-385. https://doi.org/10.1016/j.chemgeo.2004.12.019, 2005.

890   Mora, C.I., Riciputi, L.R., Cole, D.R. and Walker, K.D. High-temperature hydrothermal
891   alteration of the Boehls Butte anorthosite: origin of a bimodal plagioclase

892 assemblage. *Contributions to Mineralogy and Petrology*, *157*(6), pp.781-795.
893 https://doi.org/10.1007/s00410-008-0364-3, 2009.

894 Neusser, G., Abart, R., Fischer, F.D., Harlov, D. and Norberg, N. Experimental Na/K exchange
895 between alkali feldspar and an NaCl–KCl salt melt: chemically induced fracturing and element
896 partitioning. *Contributions to Mineralogy and Petrology*, *164*(2), pp.341-358.
897 https://doi.org/10.1007/s00410-012-0741-9, 2012.

898 Niedermeier, D.R., Putnis, A., Geisler, T., Golla-Schindler, U. and Putnis, C.V. The
899 mechanism of cation and oxygen isotope exchange in alkali feldspars under hydrothermal
900 conditions. *Contributions to Mineralogy and Petrology*, *157*(1), pp.65-76.
901 https://doi.org/10.1007/s00410-008-0320-2, 2009.

902 Norberg, N., Neusser, G., Wirth, R. and Harlov, D. Microstructural evolution during
903 experimental albitization of K-rich alkali feldspar. *Contributions to Mineralogy and*
904 *Petrology*, *162*(3), pp.531-546. https://doi.org/10.1007/s00410-011-0610-y, 2011.

905 Pessu, F., Macente, A., Sanni, O. and Piazolo, S. The importance of whole system
906 considerations for sustainable, long-term CO2 injection and storage: Interplay between
907 infrastructure-related corrosion and reservoir rock chemistry effects on the evolution of the
908 CO2 storage capacity. *International Journal of Greenhouse Gas Control*, *148*, p.104520.
909 https://doi.org/10.1016/j.ijggc.2025.104520, 2025.

910 Pinnock, S.J., Clitheroe, A.R.J. and Rose, P.T.S. The Captain Field, Block 13/22a, UK North
911 Sea. https://doi.org/10.1144/GSL.MEM.2003.020.01.35, 2003.

912 Putnis, A. Mineral replacement reactions. *Reviews in mineralogy and geochemistry*, *70*(1),
913 pp.87-124. https://doi.org/10.2138/rmg.2009.70.3, 2009.

914 Rathnaweera, T.D., Ranjith, P.G., Perera, M.S.A., Haque, A., Lashin, A., Al Arifi, N.,
915 Chandrasekharam, D., Yang, S.Q., Xu, T., Wang, S.H. and Yasar, E. CO2-induced mechanical
916 behaviour of Hawkesbury sandstone in the Gosford basin: An experimental study. *Materials*
917 *Science and Engineering: A*, *641*, pp.123-137. https://doi.org/10.1016/j.msea.2015.05.029,
918 2015.

919 Ringrose, P.: How to store CO₂ underground: Insights from early-mover CCS projects,
920 SpringerBriefs in Earth Sciences, Springer International Publishing, Cham, Switzerland, 129
921 pp., https://doi.org/10.1007/978-3-030-33113-9 , 2020.

922 Rochelle, C.A., Czernichowski-Lauriol, I. and Milodowski, A.E. The impact of chemical
923 reactions on CO2 storage in geological formations: a brief review.
924 https://doi.org/10.1144/GSL.SP.2004.233.01.07. 2004.

925 Ross, G.D., Todd, A.C., Tweedie, J.A. and Will, A.G. The dissolution effects of CO2-brine
926 systems on the permeability of UK and North Sea calcareous sandstones. In *SPE Improved Oil*
927 *Recovery Conference?* (pp. SPE-10685). SPE. https://doi.org/10.2118/10685-MS, 1982.

928 Rutter, E.H. A discussion on natural strain and geological structure-the kinetics of rock
929 deformation by pressure solution. *Philosophical Transactions of the Royal Society of London.*
930 *Series A, Mathematical and Physical Sciences*, *283*(1312), pp.203-219.
931 https://doi.org/10.1098/rsta.1976.0079, 1976.

932 Scholz, C.H. Static fatigue of quartz. *Journal of Geophysical Research*, *77*(11), pp.2104-2114.
933 https://doi.org/10.1029/JB077i011p02104, 1972.

934 Seisenbayev, N., Absalyamova, M., Alibekov, A. and Lee, W. Reactive transport modeling
935 and sensitivity analysis of CO2–rock–brine interactions at Ebeity Reservoir, West
936 Kazakhstan. *Sustainability*, *15*(19), p.14434. https://doi.org/10.3390/su151914434, 2023.

937 Shell, 2015. Peterhead CCS Project: Geochemical Reactivity Report, Doc. No.
938 PCCS-05-PT-ZR-3323-00001, produced by Shell U.K. Limited for the UK CCS
939 Commercialisation Programme, Goldeneye CO$_2$ storage project, 2015

940 Shogenov, K., Shogenova, A., Vizika-Kavvadias, O. and Nauroy, J.F. Experimental modeling
941 of CO2-fluid-rock interaction: The evolution of the composition and properties of host rocks
942 in the Baltic Region. *Earth and Space Science*, *2*(7), pp.262-284.
943 https://doi.org/10.1002/2015EA000105, 2015.

944 Stewart, N. and Marshall, J.D. The Goldeneye Field, Blocks 14/29a and 20/4b, UK North Sea.
945 https://doi.org/10.1144/M52-2018-32, 2020.

946 Summers, R. and Byerlee, J. A note on the effect of fault gouge composition on the stability of
947 frictional sliding. In *International Journal of Rock Mechanics and Mining Sciences &*
948 *Geomechanics Abstracts* (Vol. 14, No. 3, pp. 155-160). Pergamon.
949 https://doi.org/10.1016/0148-9062(77)90007-9, 1977.

950 Tullis, J. and Yund, R.A. Experimental deformation of dry Westerly granite. *Journal of*
951 *geophysical research*, *82*(36), pp.5705-5718. https://doi.org/10.1029/JB082i036p05705, 1977.

952   Wigley, M., Dubacq, B., Kampman, N. and Bickle, M. Controls of sluggish, CO2-promoted,
953   hematite and K-feldspar dissolution kinetics in sandstones. *Earth and Planetary Science*
954   *Letters*, *362*, pp.76-87. https://doi.org/10.1016/j.epsl.2012.11.045, 2013.

955   Whitney, D.L. and Evans, B.W. Abbreviations for names of rock-forming minerals. *American*
956   *mineralogist*, *95*(1), pp.185-187. https://doi.org/10.2138/am.2010.3371, 2010.

957   Wollast, R. Kinetics of the alteration of K-feldspar in buffered solutions at low
958   temperature. *Geochimica et Cosmochimica Acta*, *31*(4), pp.635-648.
959   https://doi.org/10.1016/0016-7037(67)90040-3, 1967.

960   Wheeler, J. A view of texture dynamics. *Terra Nova*, *3*(2), pp.123-136.
961   https://doi.org/10.1111/j.1365-3121.1991.tb00864.x, 1991.

962   YuanYuan, Z., QingDong, Z., Roland, H., ShanKe, L., JianMing, L. and JingBo, N., 2020.
963   Reaction mechanism during hydrothermal alteration of K-feldspar under alkaline conditions
964   and nanostructures of the produced tobermorite. *Acta Petrologica Sinica*, *36*(9), pp.2834-
965   2844. https://ui.adsabs.harvard.edu/link_gateway/2020AcPS...36.2834Y/doi:10.18654/1000-
966   0569/2020.09.14, 2020.

967   Zeitler, P.K., Enkelmann, E., Thomas, J.B., Watson, E.B., Ancuta, L.D. and Idleman, B.D.,
968   2017. Solubility and trapping of helium in apatite. *Geochimica et Cosmochimica Acta*, *209*,
969   pp.1-8. https://doi.org/10.1016/j.gca.2017.03.041, 2017.

970   Zhai, Y., Hellmann, R., Campos, A., Findling, N., Mayanna, S., Wirth, R., Schreiber, A.,
971   Cabié, M., Zeng, Q., Liu, S. & Liu, J., 2021. Fertilizer derived from alkaline hydrothermal
972   alteration of K-feldspar: micrometer to nanometer-scale investigation. *Applied Geochemistry*,
973   126, https://doi.org/10.1016/j.apgeochem.2020.104828, 2021.